iScience

CellPress
OPEN ACCESS

Article

Suv4-20h2 protects against influenza virus infection by suppression of chromatin loop formation

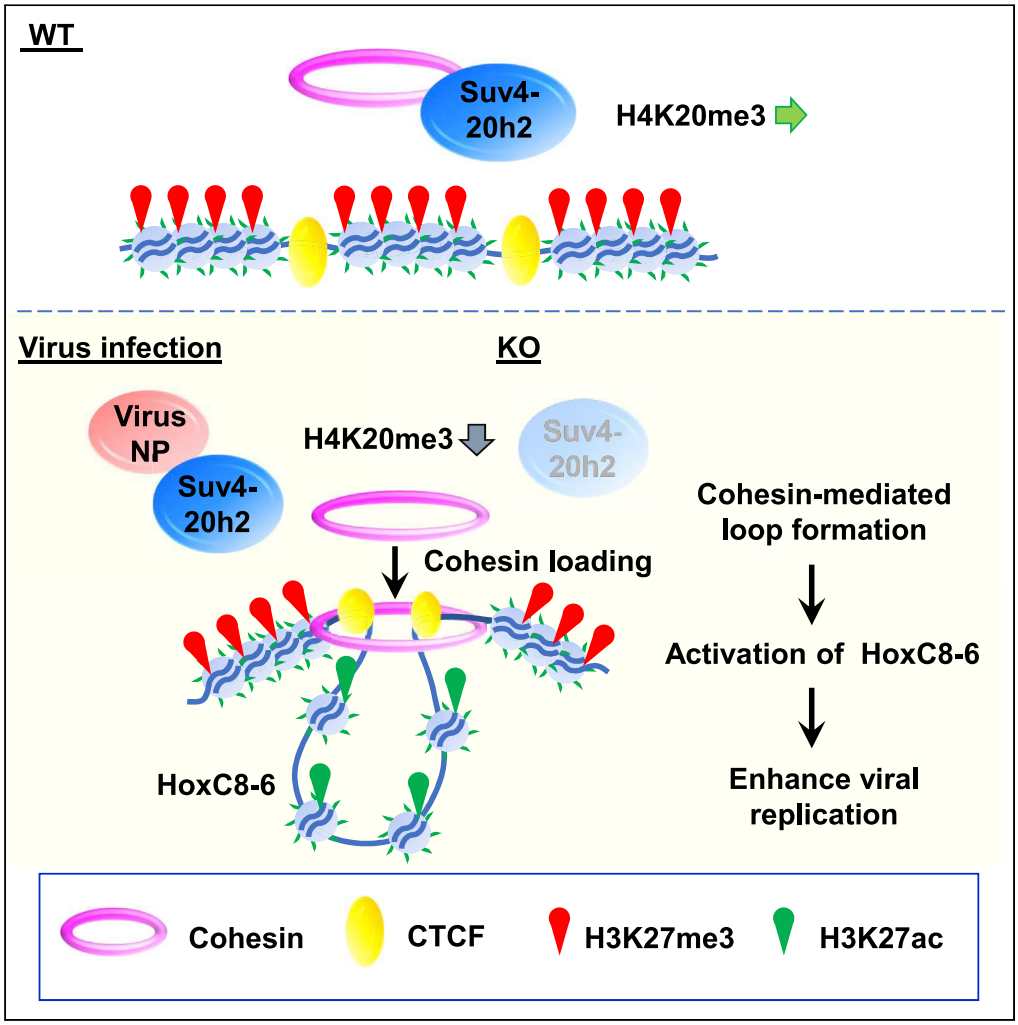

Masami Shiimori, Yu Ichida, Ryota Nukiwa, ..., Keiji Kuba, Takehiko Itoh, Yumiko Imai

y-imai@nibiohn.go.jp

Highlights

H4K20me3 methyltransferase Suv4-20h2 suppresses influenza viral replication

Influenza virus NP protein binds to Suv4-20h2 and causes dissociation from cohesin

Suv4-20h2 inactivation generates cohesion-mediated loop formation at HoxC8 -HoxC6

HoxC8-HoxC6 enhance viral replication by suppressing Wnt/β-catenin signaling

Shiimori et al., iScience 24, 102660
June 25, 2021
https://doi.org/10.1016/j.isci.2021.102660

iScience

CellPress
OPEN ACCESS

Article

Suv4-20h2 protects against influenza virus infection by suppression of chromatin loop formation

Masami Shiimori,[1,12] Yu Ichida,[1,12] Ryota Nukiwa,[1,3] Toshie Sakuma,[1] Haruka Abe,[1] Rei Kajitani,[2] Yuji Fujino,[3] Akira Kikuchi,[4] Takeshi Kawamura,[5,6] Tatsuhiko Kodama,[5] Shinichi Toyooka,[7] Katsuhiko Shirahige,[8] Gunnar Schotta,[9] Keiji Kuba,[10] Takehiko Itoh,[2] and Yumiko Imai[1,11,13,*]

SUMMARY

The spatial organization of chromatin is known to be highly dynamic in response to environmental stress. However, it remains unknown how chromatin dynamics contributes to or modulates disease pathogenesis. Here, we show that upon influenza virus infection, the H4K20me3 methyltransferase Suv4-20h2 binds the viral protein NP, which results in the inactivation of Suv4-20h2 and the dissociation of cohesin from Suv4-20h2. Inactivation of Suv4-20h2 by viral infection or genetic deletion allows the formation of an active chromatin loop at the HoxC8-HoxC6 loci coincident with cohesin loading. HoxC8 and HoxC6 proteins in turn enhance viral replication by inhibiting the Wnt-β-catenin mediated interferon response. Importantly, loss of Suv4-20h2 augments the pathology of influenza infection *in vivo*. Thus, Suv4-20h2 acts as a safeguard against influenza virus infection by suppressing cohesin-mediated loop formation.

INTRODUCTION

The linear human genome is approximately two meters long, but it is packed into cell nuclei that are only a few micrometers in diameter. Within this confined space, chromatin is 3-dimensionally (3D) organized into compartments, topologically associating domains (TADs), and loops (single interactions) that control various nuclear functions, including transcription (Gosgnach et al., 2006) (Bonev and Cavalli, 2016). The cohesin complex plays a major role in many aspects of chromosome biology, not only in sister chromatid cohesion (Guacci et al., 1997), but also in the regulation of transcription (Wendt and Peters, 2009). In parallel, nucleosomes within individual TADs or loops are marked with active (e.g., H3K27ac, H3K4me3) or repressive (e.g., H4K20me3, H3K9me3, H3K27me3) modifications, which contribute to the epigenetic regulation of transcription. The 3D structure of chromatin is known to be highly dynamic, although it remains largely unknown how chromatin dynamics contributes to or modulates the disease pathogenesis (Dekker et al., 2017).

Accumulating evidence suggests that the DNA boundary factor, CTCF, and cohesin are essential for the formation and maintenance of chromatin interaction domains, in particular of domains less than 1 Mb (Zuin et al., 2014) (Sofueva et al., 2013) (Parelho et al., 2008) (Wendt et al., 2008). According to the loop extrusion model, cohesin is crucial for forming loops by being loaded at CTCF binding sites (CTCF-BS). This is controlled by factors that regulate cohesin loading (e.g., NIPBL and MAU2) (Schwarzer et al., 2017) and unloading (e.g., WAPL and its binding partner PDS5) (Busslinger et al., 2017) (Haarhuis et al., 2017). Recent chromatin conformation capture (3C)-based techniques including 4C-seq revealed cohesin-mediated CTCF loop formation in various loci, including those of the immunoglobulin (Degner et al., 2009), β-globin (Hou et al., 2010), interferon gamma (Hadjur et al., 2009), IGF2-H19 (Nativio et al., 2009; Wendt et al., 2008) and HOXA (Wang et al., 2015) genes.

Histone lysine methyltransferase (HMT) Suv4-20h2 trimethylates H4K20, and its loss correlates with a loss of genomic integrity (Jorgensen et al., 2013), increased senescence (Nelson et al., 2016), and the upregulation of subtelomeric recombination (Benetti et al., 2007). The Suv4-20h2 protein has two functional domains, a catalytic SET domain and the Clamp domain. The SET domain catalyzes H4K20me3, while the Clamp domain is responsible for recruitment of Suv4-20h2 to pericentric heterochromatin by binding to HP1 (Hahn et al., 2013). Although Suv4-20h2 has been shown to bind cohesin and is required for chromocenter

[1]Laboratory of Regulation for Intractable Infectious Diseases, National Institutes of Biomedical Innovation, Health and Nutrition (NIBIOHN), Osaka 567-0085, Japan

[2]Department of Biological Information, School and Graduate School of Bioscience and Biotechnology, Tokyo Institute of Technology, Tokyo 152-8550, Japan

[3]Department of Anesthesiology and Intensive Care Medicine, Osaka University Graduate School of Medicine, Osaka 565-0871, Japan

[4]Department of Molecular Biology and Biochemistry, Osaka University Graduate School of Medicine, Osaka 565-0871, Japan

[5]Laboratory for Systems Biology and Medicine, Research Center for Advanced Science and Technology, the University of Tokyo, Tokyo 153-8904, Japan

[6]Proteomics Laboratory, Isotope Science Center, The University of Tokyo, Tokyo 113-0032, Japan

[7]Department of General Thoracic Surgery and Breast and Endocrinological Surgery, Okayama University Graduate School of Medicine, Okayama 700-8558, Japan

[8]Laboratory of Genome Structure and Function, Institute for Quantitative Biosciences, The University of Tokyo, Tokyo 113-0032, Japan

[9]Department of Molecular Biology, Biomedical Center, Ludwig-Maximilians-University, 82152 Munich,

Continued

clustering (Hahn et al., 2013), it is not known if the interaction between Suv4-20h2 and cohesin influences chromatin loop formation.

Influenza virus is a single-stranded RNA virus whose transcription and replication occur in the host cell nucleus by using and/or controlling host cell functions (Watanabe et al., 2010). However, the RNA genome of influenza virus does not directly integrate into the host chromatin, as does that of retroviruses (Lesbats et al., 2016) or the Epstein-Barr virus (West, 2017). Transcriptional elongation by RNA polymerase II has been shown to remodel the 3D genomic architecture during influenza virus infection (Heinz et al., 2018). However, it is unknown whether or not Suv4-20h2 is involved in the host chromatin response, or if changes in chromatin influence the pathogenesis of influenza infection.

In the present study, we show that a deficiency in Suv4-20h2 enhances both viral replication and the pathology of influenza infection *in vivo*. Earlier work has shown that the HMT Suv4-20h2 can interact with cohesin under uninfected conditions (Hahn et al., 2013). We find that upon infection, Suv4-20h2 binds the viral protein NP, which results in the inactivation of this HMT and its dissociation from cohesin. The inactivation of Suv4-20h2 by either viral infection or genetic deletion leads to active loop formation at HoxC8-HoxC6, coincident with the binding of cohesin at these sites. HoxC8 and HoxC6 expression in turn enhances viral replication by inhibiting the Wnt-β-catenin-mediated interferon response. It has been reported that patients with underlying diseases such as cancer are more likely to become severely ill from influenza or coronavirus infectious disease (e.g., COVID-19) (Hermann et al., 2017) (Kim et al., 2019) (Xia et al., 2020). Consistently, we show here that human lung cancer tissues have lower levels of H4K20me3 and Suv4-20h2, and elevated expression of HoxC6/HoxC8. Human lung cancer cells harboring these changes support enhanced viral replication. Our data thus suggest that Suv4-20h2-mediated chromatin dynamics may be responsible for the increased severity of influenza viral infection in cancer patients. Suv4-20h2 may serve as a safeguard against influenza infection by preventing cohesin-mediated changes in chromatin structure.

RESULTS

Suv4-20h2 suppresses influenza viral replication in MEFs

Suv4-20h1 and Suv4-20h2 are highly homologous enzymes that methylate histone H4K20. Suv4-20h1 is responsible for H4K20 di-methylation (H4K20me2), while Suv4-20h2 mediates tri-methylation (H4K20me3) (Schotta et al., 2008). We have examined the changes in Suv4-20h1/h2 expression and H4K20 methylation (H4K20me) during the course of influenza viral infection. The mRNA levels of Suv4-20h1 and Suv4-20h2 were not significantly changed during the time course of viral infection in mouse embryonic fibroblasts (MEFs) (Figure S2A). Similarly, Suv4-20h2 protein levels did not change substantially between uninfected and infected WT MEFs (Figure S2B). H4-tail proteomic analysis (Yamamoto et al., 2015) showed that the level of H4K20me3 in lung tissues decreased over time following influenza viral infection, while H4K20me1 or H4K20me2 levels were unchanged (Figure 1A). This was confirmed by Western blotting, which showed that in WT MEFs the level of H4K20me3, but not of H4K20me1 or H4K20me2, decreased during influenza infection (Figure S2C). We confirmed this by immunofluorescence (IF) staining of H4K20me in virus-infected WT cells (Figures 1B and S2D).

We next examined the effect of Suv4-20hr deficiency on influenza viral infection using WT, Suv4-20h1 KO (h1 KO), Suv4-20h2 KO (h2 KO) and Suv4-20h1/Suv4-20h2 double KO (dKO) MEFs. As expected, IF for H4K20me2 and H4K20me3 revealed a loss of these modifications in h1 KO and h2 KO/dKO cells, respectively (Figures 1B and S2D) (Schotta et al., 2008). Compared to WT or h1 KO cells, the h2 KO and dKO cells showed more efficient viral replication as assessed either by virus titer (Figure 1C, upper panel) or by viral NP mRNA expression (Figure 1C, lower panel). Consistently, IF for the viral NP protein showed stronger staining in h2 KO and dKO cells than in WT or h1 KO cells (Figure 1D). Similarly, by Western blot we detected higher levels of influenza viral proteins PB2, NP and M1 in virus-infected dKO vs WT MEFs (Figure 1E). Flow cytometric analysis of cell cycle stages demonstrated no major differences in the cell cycle distributions of WT and dKO cells during the influenza viral infection (Figure S1A), and viral replication was enhanced in the dKO even during G0 arrest (Figure S1B). Thus, altered cell division cycles are unlikely to influence the observed changes.

Influenza virus interacts with the SET domain of Suv4-20h2 and reduces its H4K20me3 activity

To determine which domain of Suv4-20h2 is critical for suppressing viral replication, we generated dKO cells into which we transduced viral vectors expressing the EGFP-tagged full length Suv4-20h2 (h2-FL),

Germany; Munich Center for Integrated Protein Science (CiPS), 81377 Munich, Germany

[10]Department of Biochemistry and Metabolic Science, Akita University Faculty of Medicine, Akita 010-8543, Japan

[11]Laboratory for Infectious Systems, Institute for Protein Research, Osaka University, Osaka 565-0871, Japan

[12]These authors contributed equally

[13]Lead contact

*Correspondence: y-imai@nibiohn.go.jp

https://doi.org/10.1016/j.isci.2021.102660

its SET domain (h2-SET), or Clamp domain (h2-Clamp), or an empty vector (EV; Figure S3A). The cells were subsequently infected with influenza virus. h2-EGFP and virus NP protein were stained and visualized, and we quantified the percentages of NP-positive cells among all h2 EGFP-positive cells in these images. The percentage of NP positive cells was reduced in dKO MEFs expressing h2-FL or h2-SET domains, as compared to the h2-Clamp domain (Figure 2A). In addition, virus titers and NP expression were attenuated in dKO cells overexpressing Suv4-20h2 (Figure 2B). Thus, our data suggest that Suv4-20h2, and in particular the SET domain of Suv4-20h2, can suppress the replication of influenza virus.

Although specific interactions between influenza virus (e.g., NP, PB2) and host proteins have been reported in the nucleus (Garcia-Robles et al., 2005), it was not known whether these viral proteins bind Suv4-20h2 in virus-infected cells. To test this, first we established the dKO MEFs expressing AM-tagged Suv4-20h2. Using the cells infected with influenza virus, we performed immunoprecipitation (IP) with anti-AM Ab, and the IP products were subjected to stable isotope labeling (SILAC) and LC-MS/MS analysis. As shown in Figure 2C, viral proteins NP and PB2, but not other viral proteins, co-precipitated with Suv4-20h2. We then used Suv4-20h2^{Flag} knock-in mouse embryonic stem (mES) cells and performed an IP with Flag Ab. Again, the Western blot analysis showed that viral proteins NP and PB2, but not M1, were recovered with Suv4-20h2 (Figure 2D). Finally, GST pull-down assay using three different truncation proteins of Suv4-20h2, namely, the full length (FL), SET domain (SET), and Clamp domain (Clamp; Figure S3A), confirmed that the NP and PB2 proteins could bind the FL and SET domains of Suv4-20h2 (Figure S3B). As previously described, HP1α was able to bind uniquely to the Clamp domain of Suv4-20h2 (Hahn et al., 2013) (Hahn et al., 2013) (Hahn et al., 2013).

We next tested for direct interactions between Suv4-20h2 and viral proteins *in vitro*. We purified recombinant viral NP and PB2 proteins, as well as the host cell HP1α, and GST-fusions to Suv4-20h2 FL, SET, or Clamp domain proteins. Pull-down assays with GST-fused Suv4-20h2 confirmed that viral NP and PB2 proteins bound the full length Suv4-20h2 and its SET domain (Figure 2E). Furthermore, 293T cells expressing flag-tagged NP protein were fractionated into nuclear Fractions I and II, which were enriched for euchromatin-associated proteins (Fraction I) and heterochromatin-associated proteins (Fraction II), respectively. Following IP with Flag Ab which precipitates NP, we detected the co-IP of Suv4-20h2 in Fraction II only (Figure S3C). Collectively, these data indicated that influenza virus proteins interact with Suv4-20h2, and in particular with its SET domain, both *in vivo* and *in vitro*.

We next examined whether the interaction between the viral NP and the SET domain of Suv4-20h2 altered the enzyme's ability to generate H4K20me3. To test this, we performed a H4K20 methylation assay *in vitro* by co-incubating nucleosomes and the recombinant human Suv4-20h2 SET domain, with or without viral NP or M1 protein. The addition of NP, but not M1, reduced the efficiency of Suv4-20h2-mediated H4K20 trimethylation (Figure 2F), suggesting that the viral NP is able to attenuate the H4K20me3 HMT activity of Suv4-20h2.

Cohesin is dissociated from Suv4-20h2 upon influenza virus infection

Next, we examined the interaction between Suv4-20h2 and host nuclear proteins using dKO MEFs expressing AM-tagged Suv4-20h2. Soluble and insoluble chromatin fractions I and II were isolated from the cells followed by DNA digestion by benzonase. Since AM-tagged Suv4-20h2 was detected in Fraction II, this fraction was subjected to IP with AM Ab using both non-infected and infected dKO MEFs expressing AM-tagged Suv4-20h2. dKO cells that do not express the tagged Suv4-20h2 were used as a negative control. The input and IP proteins were subjected to LC-MS/MS proteomics analysis, and showed that cohesin (e.g., Rad21, Smc1, Smc3), CTCF, Nup98, and LaminB1, all co-precipitated with Suv4-20h2 (Figure S4A). Their recovery was confirmed by Western blotting (Figure 3A). Upon viral infection, the Suv4-20h2 interactions with Rad21 and Smc1, but not with Smc3, were suppressed (Figure 3A, left panel and Figure S4A). We then performed an inverse IP with anti-Rad21 from extracts of the dKO MEFs expressing AM-tagged Suv4-20h2. We found that Suv4-20h2 and Wapl co-precipitated with Rad21, and that the interaction of Rad21 with Suv4-20h2, but not with Wapl, was reduced by influenza viral infection (Figure 3B). Indeed, using WT and dKO MEFs the binding of Rad21 to Wapl was shown to be comparable in WT and dKO cells (Figure S4B).

We next performed GST pull-down with GST-fused to FL, the SET domain or Clamp domain of Suv4-20h2, from nuclear extracts isolated from infected or uninfected WT cells. Ezh2, Lamin B1, and Rad21 were all able to bind the FL and SET domains of Suv4-20h2 (Figure 3C), but only binding to Rad21 was compromised

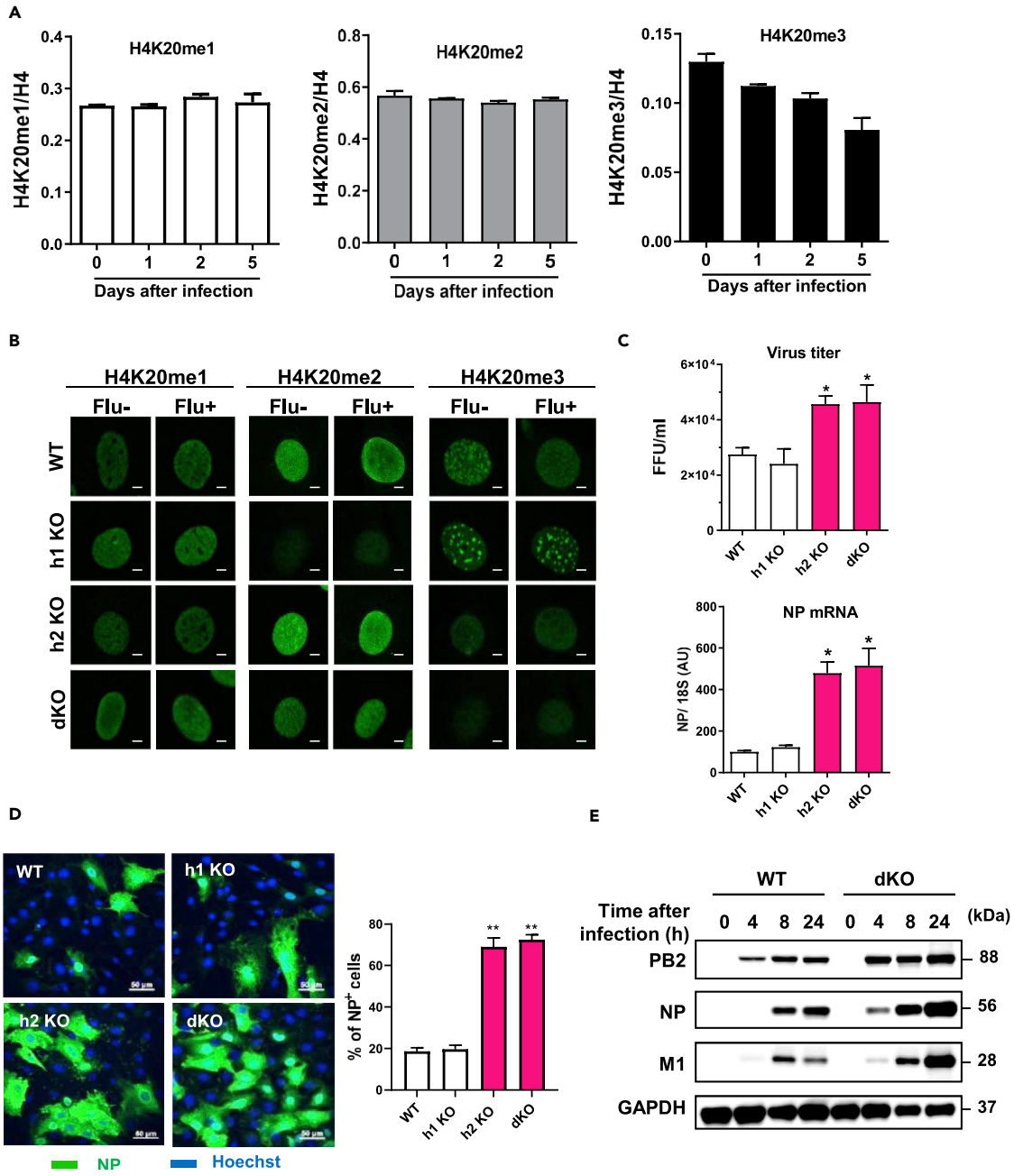

Figure 1. Deletion of Suv4-20h2 enhances influenza viral replication

(A) WT mice were intratracheally infected with influenza virus (PR8 virus, 100 FFU), and lung tissues were sampled at the indicated time points. Histone was extracted from the lung tissues and was subjected to H4-tail proteomics analysis. Relative expression levels of H4K20me1, H4K20me2, and H4K20me3 to H4 were shown (n = 5 per group).

(B–D) MEFs obtained from WT, Suv4-20h1 KO (h1 KO), Suv4-20h2 KO (h2 KO) and Suv4-20h1/Suv4-20h2 double KO (dKO) mice were infected with mock (Flu-) or influenza virus (MOI: 0.5) (Flu+). Cells were fixed and stained with either H4K20me1, H4K20me2 or H4K20me3 Abs, and Hoechst. Data are from three separate experiments. Representative staining is shown. Scale bars: 10 μm (B). Culture supernatant and cells were sampled at 8 hr after infection. Virus titer assessed by FFU in supernatant is shown (C, upper panel). NP mRNA expression of the cells is shown (C, lower panel). Data are from three separate experiments. *$p < 0.05$ compared to WT. Infected cells were fixed, and virus NP protein was stained (green). Nuclei were counterstained with Hoechst (blue). Representative staining is shown. Scale bars: 50 μm (D, left panel). The percentages of NP-positive in total of Hoechst positive are shown (D, right panel). **$p < 0.01$ compared to WT.

Figure 1. *Continued*

(E) WT and dKO MEFs were infected with influenza virus (MOI: 0.5) and sampled at the indicated time point. Western blots of virus PB2, NP and M1 proteins, along with GAPDH are shown.

Data were reproduced in three experiments. The data in (A, C and D) (right panel) are presented as means ± s.e.m.. Statistical analysis were carried out using analysis of variance with Bonferroni post t tests.

in virus-infected nuclear lysates (Figure 3C). In contrast, the binding of HP1α and HP1β to the Clamp domain of Suv4-20h2, was unchanged upon infection (Hahn et al., 2013). We note that the expression of PRC2 (e.g., Ezh2), heterochromatin associated proteins (e.g. HP1α, Lamin B1, Nup98, Nup153) and loop-associated proteins (e.g., Nipbl, Wapl, Pds5b, Rad21, CTCF), were all comparable in both WT and dKO cells, and did not vary upon infection (Figure S4C). We conclude that the deletion of Suv4-20h2 has no significant effect on the levels of PRC2, heterochromatin-associated proteins, and chromatin loop-forming proteins, but cohesin (as monitored by Rad21) was selectively dissociated from Suv4-20h2 upon influenza virus infection. Wapl, which is a known cohesin-unloading factor, was able to bind cohesin, but not Suv4-20h2, and the Wapl-cohesin interaction was unchanged by virus infection.

Inactivation of Suv4-20h2 activates C9|8 to C6|5 region at HoxC cluster

We next examined transcriptional changes in WT and dKO cells with and without virus infection. Our microarray data showed that HoxC8 was the most highly upregulated gene in dKO cells (Figure S5A). Consistent with this, RT-qPCR demonstrated a strong induction of HoxC8, HoxC6, and a weaker upregulation of HoxC5, in h2 KO and dKO MEFs with or without viral infection (Figure 4A). On the other hand, WT cells showed a weak upregulation of HoxC8, HoxC6, and HoxC5 loci only after virus infection. Since the population of cells after viral infection contains both virus (NP)-positive and -negative cells, we sorted the NP-positive and NP-negative cell populations. As shown in Figure 4B, mRNA expression of HoxC8, HoxC6, and HoxC5 was more strongly upregulated in the NP-positive (Flu+) than in NP-negative (Flu-) WT cells.

To examine the Suv4-20h2 binding, using the dKO cells expressing AM-tagged Suv4-20h2, we performed ChIP-seq with anti-AM Ab. We did not detect a significant peak of Suv4-20h2 binding in the HoxC region, but the dispersed signal was slightly reduced following infection (Figure S6A). ChIP-seq for H4K20me3 also showed no specific peaks in the HoxC region in WT cells, although H4K20me3 levels were generally reduced by infection (Figures S6A and S6B). The reduction in H4K20me3 ChIP signal across the HoxC locus following viral infection was more readily detected by ChIP-qPCR, and all H4K20me3 signal was lost in dKO cells due to HMT ablation (Figure 4C). The lack of Suv4-20h2 and H4K20me3 peaks at HoxC5-C8 loci make it unlikely that these directly regulate the selective expression of HoxC8, HoxC6 and HoxC5 in dKO or in virus-infected WT cells.

Since Suv4-20h2 interacts with Ezh2, a core subunit of PRC2 (Figures 3A and 3C), we next examined the distribution of H3K27me3, the catalytic product of Ezh2. We performed ChIP with H3K27me3 using the Flu-, NP-negative and the Flu+, NP-positive, WT and dKO cells, sorted as described above. The H3K27me3 modification mapped across the entire HoxC cluster in the Flu-, NP-negative WT cells (Figure 4D), yet the signal was decreased across HoxC8-HoxC5 in the Flu+, NP-positive WT cells (Figure 4D). Similarly, in the dKO cells with or without viral infection, H3K27me3 signal was lost from the HoxC8 through the HoxC4 loci (Figure 4D). In contrast, H3K27ac was found highly enriched on HoxC8, HoxC6 and HoxC5 loci in the Flu + NP-positive WT and the dKO cells, independent of infection (Figure 4E), whereas it disappeared in the Flu-, NP-negative WT cells. Thus, the distributions of the repressive H3K27me3 mark and the active H3K27ac modification were similar in the virus-infected WT cells (i.e., Flu+, NP-positive) and in dKO cells, although the dynamic range was much more pronounced in cells lacking Suv4-30 HMTs. We note that ChIP-qPCR in unsorted cells showed the repressive H3K27me3 mark across the entire HoxC cluster in WT cells, whereas it was restricted to HoxC13-HoxC9 in h2 KO and dKO cells (Figure S7A). The active H3K27ac mark, on the other hand, localized to HoxC8, HoxC6, and HoxC5 loci in h2 KO, dKO, and in virus-infected WT cells (Figure S7B). In ChIP-seq using unsorted cells the differences between WT, Flu- and WT, Flu+ were not significant (Figure S6A). We also examined the distribution of the chromatin architectural protein CTCF and cohesion subunit Rad21 by ChIP-seq on unsorted cells. Both were recovered in the intergenic region between HoxC9 and HoxC8 (C9|8) and between HoxC6 and HoxC5 (C6|5) at CTCF-BS, in WT and dKO cells independent of infection status (Figure S6A). Thus, inactivation of Suv4-20h2 by viral infection or by gene deletion both showed a specific

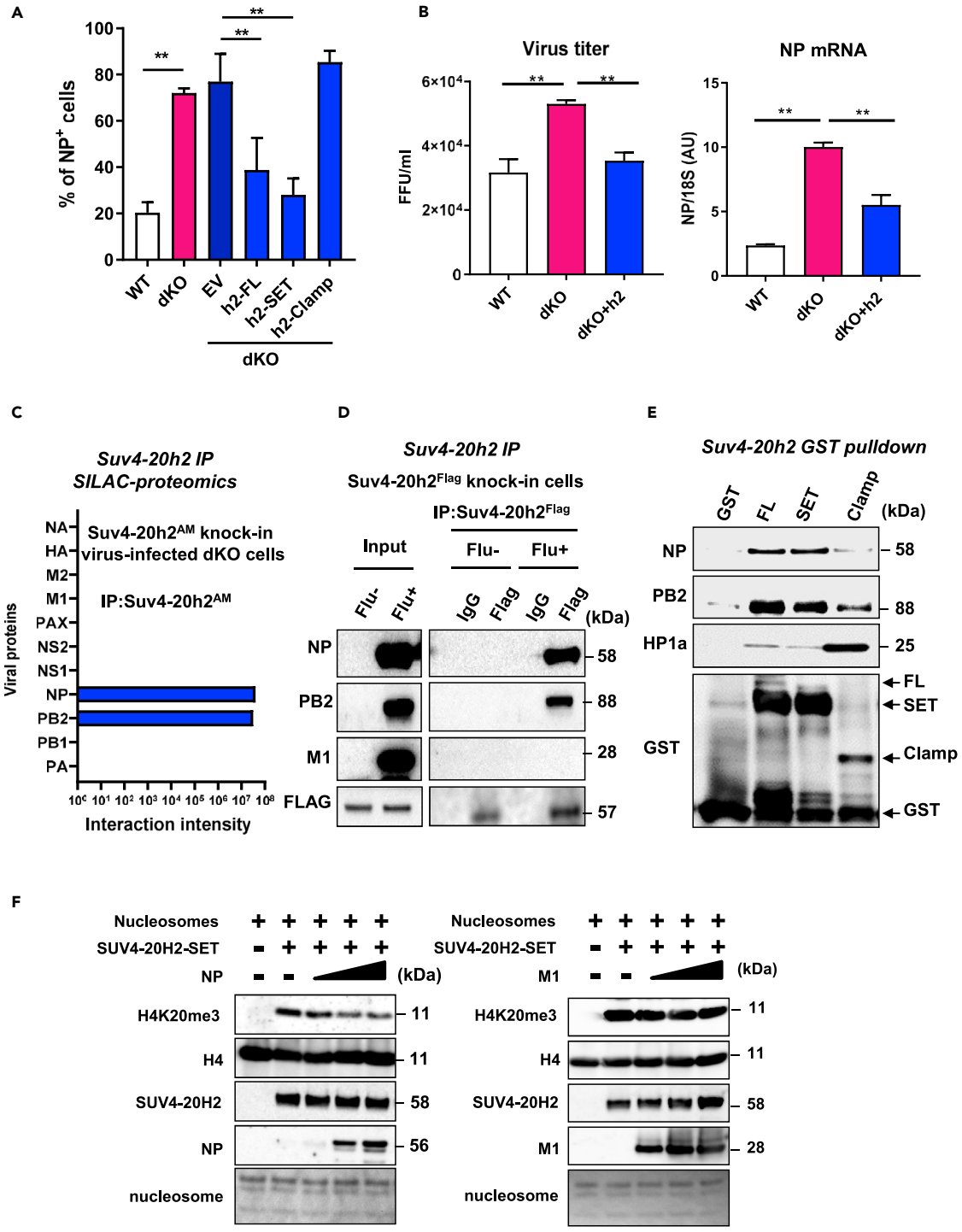

Figure 2. Suv4-20h2 interacts with virus and host nuclear proteins

(A) dKO cells transduced with EGFP-tagged empty vector (EV), Suv4-20h2 full length (h2-FL), SET domain (h2-SET) or Clamp domain (h2-Clamp; left panel) were infected with influenza virus (MOI: 0.5) for 8 hr h2-EGFP and virus NP protein were co-stained. Nuclei were counterstained with Hoechst. The percentages of NP-positive in total of the h2 EGFP-positive are shown. Data are from three separate experiments. **P < 0.01 between the groups.

(B) WT, dKO, and dKO MEFs overexpressed with Suv4-20h2 were infected with influenza virus (MOI: 0.5). Culture supernatant and cells were sampled at 8 hr after infection. Virus titer of FFU in supernatant is shown (B, left panel). NP mRNA expression of the cells is shown (B, right panel). Data are from three separate experiments. *p < 0.05, **p < 0.01 between the groups.

Figure 2. *Continued*

(C) dKO MEFs transduced with AM-tagged Suv4-20h2 were infected with influenza virus (MOI: 0.5) for 8 hr. Nuclear extracts were prepared from the cells, and were immunoprecipitated (IP) with AM Ab, and IP product was subjected to a stable isotope labeling (SILAC) & LC-MS/MS analysis. Virus NP and PB2 proteins were identified in this analysis.

(D) Suv4-20h2^{Flag} knock-in mouse embryonic stem (mES) cells were mock (Flu-) or infected with influenza virus (MOI: 0.5) (Flu+) for 8 hr. Nuclear extracts were prepared from the cells, and were immunoprecipitated with Flag Ab. Western blotting shows that virus NP and PB2 proteins were co-precipitated with Suv4-20h2. Data were reproduced in three experiments.

(E) Purified recombinant viral NP and PB2 proteins and GST-fusion proteins to full length (FL), SET, and Clamp domain of Suv4-20h2, were used in a pull-down assay. Virus NP and PB2 proteins interacted with FL and SET domain of Suv4-20h2. Data were reproduced in three experiments.

(F) Human SET domain of SUV4-20H2 (2-281) was pre-incubated with virus NP protein (0, 0.05, 0.5, or 1.0 μg) (left panel) or M1 protein (0, 0.05, 0.5, or 1.0 μg) (right panel) at room temperature for 1hr and then incubated with polynucleosomes (1.0 μg) for additional 3hr. Protein samples were subjected to Western blot analysis using specific antibodies. H4K20me3 was suppressed in a dose-dependent manner by NP protein.

Data were reproduced in three experiments. The data in (A and B) are presented as means ± s.e.m.. Statistical analysis were carried out using analysis of variance with Bonferroni post t tests.

shift in active (H3K27ac) and repressive (H3K27me3) histone marks on the HoxC cluster, resulting in the selective activation of the C9|8 to C6|5 region.

Inactivation of Suv4-20h2 generates cohesin-mediated loop at C9|8 to C6|5 region of HoxC cluster

As shown in Figure 3A, cohesin (i.e., Rad21 and Smc1) lose binding to Suv4-20h2 upon virus infection. To examine the possible involvement of CTCF and cohesin in the response monitored at the HoxC loci, we performed ChIP-qPCR with appropriate antibodies. We found that CTCF bound equally well to CTCF BS at C12|11, C9|8 and C6|5 in uninfected and virus-infected WT and dKO cells (Figure 5A). Importantly, the binding of Rad21 (Figure 5B) and Smc1 (Figure 5C) to the putative loop boundaries (C9|8 and C6|5) increased significantly in dKO and virus-infected WT cells, while binding to C12|11 was not substantially changed. The binding of Wapl to the loop boundaries (C9|8 and C6|5) resembled that of Rad21 (Figure 5D), suggesting that Wapl may not be acting as a cohesin unloading factor at these sites. Using the dKO cells expressing full length of Suv4-20h2, we asked if the restoration of Suv4-20h2 expression would suppress cohesin loading at the loop boundaries in dKO cells. As shown in Figure 5E, dKO cells expressing full length of Suv4-20h2 failed to increase cohesin loading at the CTCF-BS sites (C9|8 and C6|5), suggesting that Suv4-20h2 indeed inhibits cohesin loading at CTCF-BS. Moreover, using the dKO MEF cells expressing the EGFP-tagged full length (h2-FL), SET domain (h2-SET), or Clamp domain (h2-Clamp) Suv4-20h2 protein, or empty vector (EV; Figure S3A), we found that the upregulation of HoxC8 and HoxC6 mRNAs in dKO cells was suppressed by the over-expression of FL Suv4-20h2 or its SET domain (Figure 5F). This strongly suggests that the inactivation of HoxC8 and HoxC6 depends on the Suv4-20h2 SET domain, and that this anti-correlates with the recruitment of cohesin to specific CTCF-BS sites (C9|8 and C6|5). Taken together, our data indicate that Suv4-20h2 essentially acts as an alternative cohesin unloading factor at specific regions (HoxC8-HoxC6). Inactivation of Suv4-20h2 by influenza viral infection or genetic deletion resulted in enhanced cohesin loading at CTCF-BS, and Hox gene upregulation.

Next, we examined whether an active chromatin loop might form in the C9|8 to C6|5 region (around 20kb) upon the inactivation of Suv4-20h2. To test this, we performed 4C-seq in uninfected or infected WT and dKO cells, which enables the high-resolution identification of interactions between one locus (e.g., viewpoint) and all other genomic loci. Using viewpoints located within either the transcriptionally active (HoxC8) (Figure S8A) or repressive (HoxC12) (Figure S8B) region, we showed that there was an interaction between HoxC8 and HoxC6 in dKO cells. Of note, this interaction was almost absent in uninfected WT cells, whereas it was slightly increased in the virus-infected WT cells (Figure S8A). To further examine whether we can monitor a change in 3D organization consistent with an active chromatin loop spanning the 20kb from C9|8 to C6|5 sites upon the inactivation of Suv4-20h2, we performed DNA FISH in WT and dKO cells, coupled with the immunostaining of virus NP protein to identify those that are uninfected (Flu-) and virus-infected (Flu+). In uninfected WT cells, the HoxC8-6 region was found close to the nuclear membrane, like the HoxC13-12 region (Figure S9). This is consistent with low level expression. The distance between HoxC8-6 and the nuclear envelope increased significantly in virus-infected NP-positive WT cells and in dKO cells (Figures S9A and S9B). In contrast, the region of HoxC13-12 remained near the nuclear membrane in both uninfected and infected WT and dKO cells (Figures S9C and S9D).

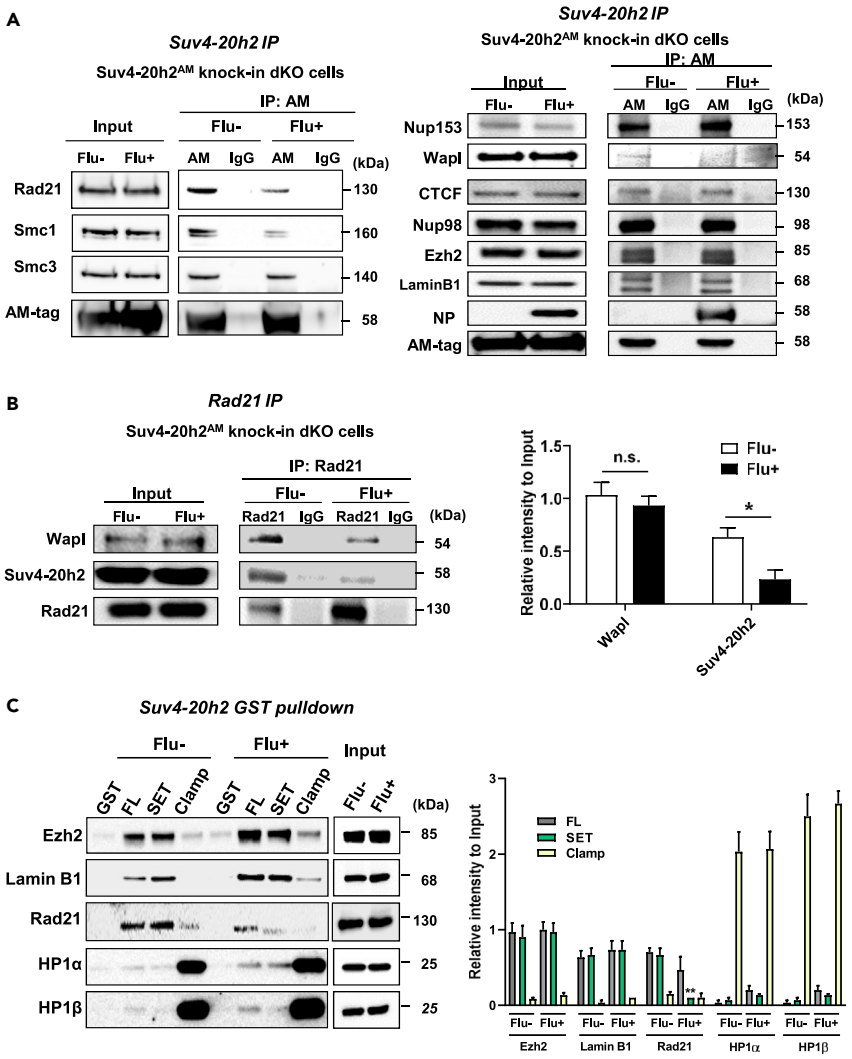

Figure 3. Cohesin is dissociated from Suv4-20h2 upon influenza virus infection

(A) dKO MEFs transduced with AM-tagged Suv4-20h2 were mock (Flu-) or infected with influenza virus (MOI: 0.5) (Flu+) for 8 hr. Nuclear fraction I and II were prepared from the cells. Fraction II was subjected to IP with anti-AM Ab. Western blotting of the IP products is shown. Cohesin (Rad21, Smc1, Smc3) was immunoprecipitated with Suv4-20h2, and interaction of Suv4-20h2 to Rad21 or Smc1 was suppressed upon infection (left panel). Nup153, CTCF, Nup98, Ezh2, and Lamin B1, rather than Wapl were co-precipitated with Suv4-20h2 (right panel). Data were reproduced in four experiments.

(B) dKO MEFs transduced with AM-tagged Suv4-20h2 were mock (Flu-) or infected with influenza virus (MOI: 0.5) (Flu+) for 8 hr. Nuclear fractions I and II were prepared from the cells, and Fraction II was subjected to anti-Rad21 IP. Western blotting of the IP products is shown. Rad21 was co-precipitated with Wapl and Suv4-20h2 under non-infected conditions, and interaction of Rad21 and Suv4-20h2 was suppressed upon viral infection. Protein level was quantified by WB densitometry and relative intensity of Wapl and Suv4-20h2 to Input are shown (right panel). Not significant (n.s.), *$P < 0.05$ between the groups. Data are from two three separate experiments.

(C) GST-fused proteins to full length Suv4-20h2 (FL), and to its SET and Clamp domains were purified, and were subjected to pull-down with nuclear lysates obtained from mock (Flu-) or virus-infected (Flu+) cells. Western blots of Ezh2, Lamin B1, Rad21, HP1α, and HP1β are shown (left panel). Relative intensity to Input are shown (right panel). Interaction of Rad21 and SET domain of Suv4-20h2 was suppressed in the virus-infected cells. **$P < 0.01$ between the groups.

Data are from three separate experiments. The data in (B) (right panel) and (C) (right panel) are presented as means ± s.e.m. Statistical analysis were carried out using unpaired t test.

Taken together, our data suggest a 3D change in chromatin conformation, coincident with increased cohesin loading at the CTCF-BS of C9|8 and C6|5, generating an active chromatin loop in Flu + WT and dKO cells (Figure S10).

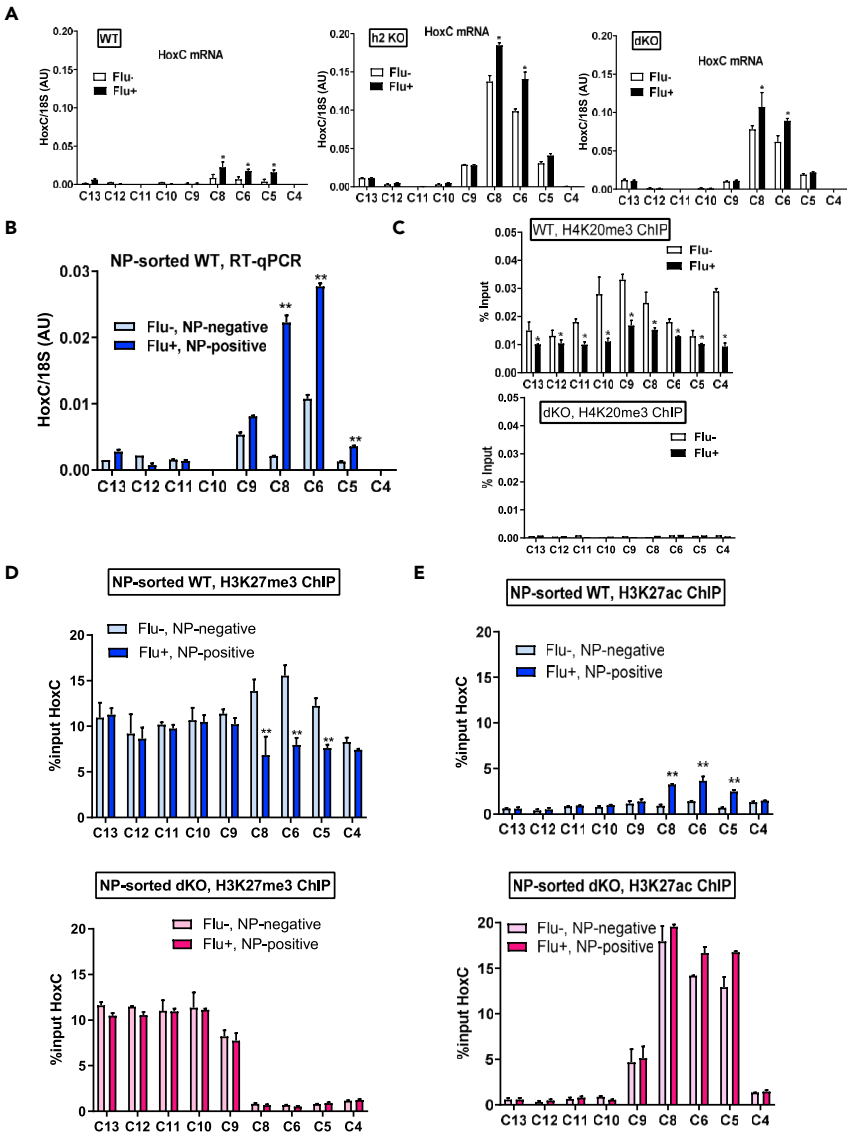

Figure 4. Loss of Suv4-20h2 or viral infection activates HoxC8, HoxC6 and HoxC5

(A) WT, h2 KO and dKO MEFs were infected with mock (Flu-) or influenza virus (MOI: 0.5; Flu+) for 8 hr mRNA expression of genes of the HoxC cluster are shown. *P < 0.05 compared to Flu-. Data are from five separate experiments.

(B) WT MEFs were infected with mock (Flu-) or influenza virus (MOI: 0.5) (Flu+) for 8 hr, and NP-negative or NP-positive cells were sorted. mRNA expression of HoxC cluster was shown. **P < 0.01 compared to Flu-, NP-negative cells. Data are from three separate experiments.

(C) WT and dKO MEFs were mock (Flu-) or infected with influenza virus (MOI: 0.5; Flu+) for 8 hr, followed by ChIP with anti-H4K20me3.

(D and E) WT and dKO MEFs were infected with mock (Flu-) or influenza virus (MOI: 0.5; Flu+) for 8 hr, and NP-negative or NP-positive cells were sorted. H3K27me3 ChIP-qPCR (D) and H3K27ac ChIP-qPCR (E) on HoxC cluster using the sorted cells are shown. **P < 0.01 compared to Flu-, NP-negative cells.

Data are from three separate experiments. The data in (A–E) are presented as means ± s.e.m. Statistical analysis were carried out using unpaired t test.

HoxC8 and HoxC6 enhance viral replication through the suppression of Wnt/β-catenin mediated interferon signaling

We next examined how the enhanced expression of HoxC8 and HoxC6 contributes to enhanced influenza viral replication. Knockdown of HoxC8, HoxC6, or HoxC8 and HoxC6 by siRNA substantially attenuated viral replication, as assessed by viral NP mRNA expression in dKO MEFs (Figure 6A and S11A). This suggests that HoxC8

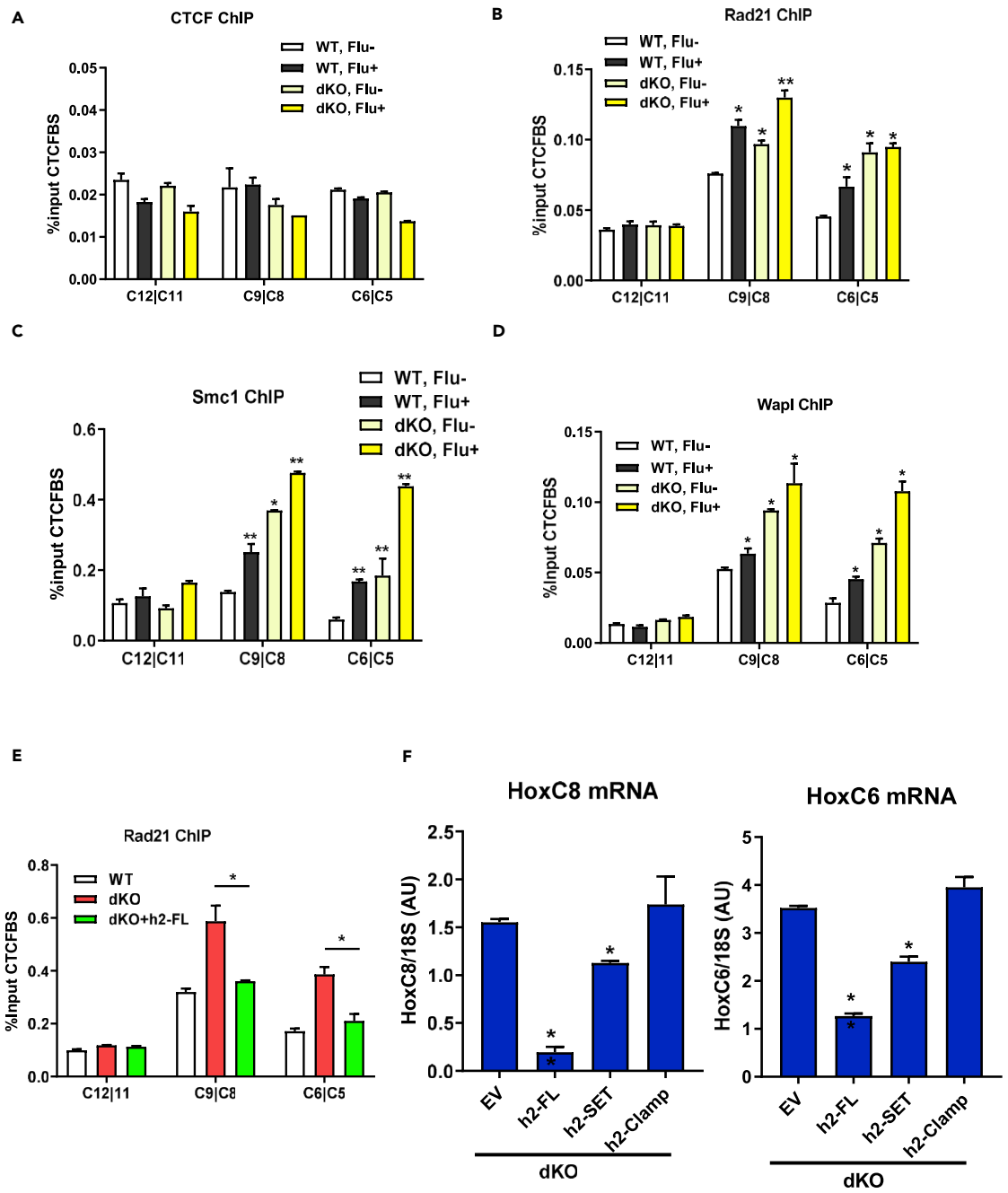

Figure 5. Loss of Suv4-20h2 or viral infection generates a cohesin-mediated active loop at HoxC cluster

(A–D) WT and dKO MEFs were mock (Flu-) or infected with influenza virus (MOI: 0.5) (Flu+) for 8 hr. ChIP-qPCR with CTCF (A), Rad21 (B), Smc1 (C), or Wapl (D) was performed. The data of binding to HoxC CTCF-BS at C12|C11, C9|8, and C6|5 are shown. Data are from three separate experiments. *$p < 0.05$, **$p < 0.01$ compared to WT, Flu-.

(E) Using WT, dKO, and dKO expressing full length of Suv4-20h2 cells, ChIP-qPCR with anti-Rad21 was performed. Rad21 binding to CTCF-BS at C12|C11, C9|8, and C6|5 are shown. *$p < 0.05$ between the groups. Data are from three separate experiments.

(F) Empty vector (EV), and vectors expressing full length Suv4-20h2 (FL), or its SET and Clamp domains were stably introduced into dKO MEFs. HoxC8 (left panel) and HoxC6 (right panel) mRNA expression of the indicated cells are shown. *$p < 0.05$ compared to EV.

Data are from three separate experiments. The data in (A–F) are presented as means ± s.e.m. Statistical analysis were carried out using unpaired t test analysis of variance with Bonferroni post t tests.

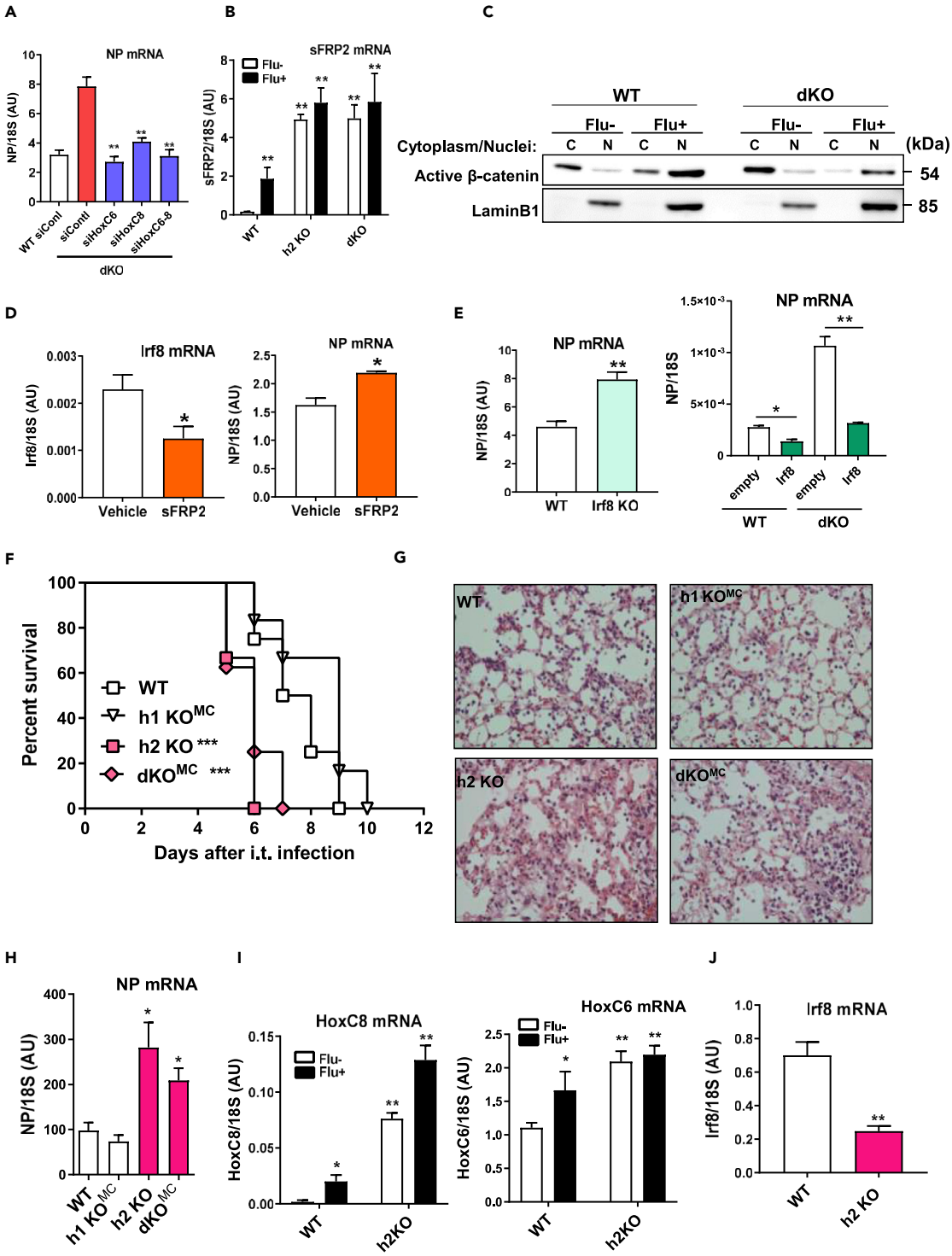

Figure 6. HoxC8 and HoxC6 enhances viral replication through suppression of Wnt/β-catenin mediated interferon signaling and deletion of Suv4-20h2 aggravates the pathology of influenza in mice

(A) WT MEFs knocked down by control siRNA, and dKO MEFs knocked down by control, HoxC8, HoxC6, or HoxC8 and HoxC6 siRNA, were infected with influenza virus (MOI: 0.5) for 8 hr. Viral NP mRNA expression is shown. Data are from three separate experiments. **p < 0.01 compared to dKO knocked down by control siRNA.

(B) WT, h2 KO, and dKO MEFs were infected with mock- (Flu-) or influenza virus (MOI: 0.5; Flu+) for 8 hr mRNA expression of sFRP2 is shown. **p < 0.01 compared to WT Flu-.

Figure 6. *Continued*

(C) WT or dKO cells were infected with mock- (Flu-) or influenza virus (MOI: 0.5; Flu+) for 8 hr, and cytoplasmic (C) and nuclear (N) fractions were isolated. Western blots of active β-catenin and LaminB1 are shown. Data were reproduced in three experiments.

(D) WT MEFs were treated with vehicle or recombinant mouse sFRP2 protein, followed by influenza viral infection (MOI: 0.5) for 8 hr mRNA expression of Irf8 (left panel), and NP (right panel) is shown. *p < 0.05 compared to vehicle control.

(E) WT, Irf8 KO MEFs were infected with influenza virus (MOI: 0.5; Flu+) for 8 hr. NP mRNA expression is shown (E, left panel). Data are from three separate experiments. **p < 0.01 compared to WT. WT and dKO MEFs were transduced with empty or Irf8 vector, and infected with influenza virus (MOI: 0.5) for 8 hr. NP mRNA expression of the cells is shown (E, right panel). Data are from three separate experiments. **p < 0.01 and *p < 0.05 between the groups.

(F–H), WT, macrophage-specific Suv4-20h1 KO (h1 KO^{MC}), Suv4-20h2 KO (h2 KO), and macrophage-specific Suv4-20h1 and Suv4-20h2 double KOs (dKO^{MC}) mice, were intratracheally infected with influenza virus (PR8 virus, 100 FFU). The survival after infection is shown. n = 7–8 per group (F). p***<0.0001 compared to WT. Statistical analysis were carried out using Bonferroni post t tests. In a separate experiment, lung tissues were sampled at 5 days after infection, and lung histology (G) and virus NP mRNA expression (H) are shown. n = 5–7 per group. *p < 0.05 compared to WT.

(I and J) WT and h2 KO mice were intratracheally infected with influenza virus (PR8 virus, 100 FFU), and lung tissues were sampled at day 0 (Flu-) and day2 (Flu+) after infection. n = 6 per group. mRNA expression of HoxC8 (I, left panel) and HoxC6 (I, right panel) of lung tissues are shown. *p < 0.05, **p < 0.01 compared to WT, Flu-. Irf8 mRNA expression in virus infected lung tissues is shown (J). **p < 0.01 compared to WT.

The data in (A–E), and (H–J) are presented as means ± s.e.m. Statistical analysis were carried out using unpaired t test for (D, E and J) and analysis of variance with Bonferroni post t tests for (A, B, H and I)

and HoxC6 proteins help regulate viral replication. Recent studies have shown that Wnt-β catenin signaling is regulated by HoxC8, and vice versa (Lei et al., 2006) (Lei et al., 2005). Consistent with this, our transcriptome data showed that genes of the Wnt-β catenin pathway, like secreted frizzled-related protein 2 (sFRP2), are strongly upregulated in the Suv4-20 dKO (Figure S5A). sFRP2 is known to suppress Wnt signaling by sequestering Wnt through its Cysteine-rich domain, or by acting as dominant-negative inhibitor (Kaur et al., 2016; Klaus and Birchmeier, 2008). Consistent with the notion that HoxC8/C6 might regulate Wnt-β catenin signaling, sFRP2 expression was increased in h2KO and dKO cells, as well as in virus-infected WT MEFs (Figure 6B). Importantly, the knockdown of HoxC8, HoxC6, or HoxC8 and HoxC6 by siRNA attenuated the expression of sFRP2 in dKO MEFs (Figure S11B), placing the Hox genes between Suv4-20h2 and Wnt/β-catenin targets.

Other studies have shown that β-catenin inhibits influenza viral replication by promoting an interferon (IFN) response (Hillesheim et al., 2014). β-catenin functions as a transcriptional regulator of gene expression in association with members of the T cell factor/lymphoid enhancer factor (Tcf/Lef1) family of transcriptional regulators (Cadigan and Waterman, 2012). A recent study has shown that interferon-regulatory factor 8 (Irf8) promoter regions contain three consensus-binding sites for Tcf/Lef1 (Tcf/Lef1-binding elements, CTTTGAT and ATCAAAG, respectively) in a region 1.7 kb upstream of the transcriptional start site, arguing that Irf8 could be a target of Wnt-β-catenin signaling (Scheller et al., 2013). Thus, we wondered if HoxC8-C6 might also enhance viral replication through inhibition of β-catenin-Irf8 signaling.

To test this, we first examined the nuclear translocation of active β-catenin in uninfected and infected WT and dKO MEFs. Active β-catenin was accumulated in the nucleus following influenza viral infection in WT MEFs, as previously reported (Hillesheim et al., 2014). However, the nuclear accumulation of active β-catenin was reduced in virus-infected dKO MEFs (Figure 6C). Furthermore, when we treated WT cells with vehicle or recombinant mouse sFRP2 protein, followed by mock- or influenza viral infection, we found that β-catenin nuclear translocation was reduced in the sFRP2-treated virus-infected cells (Figure S11C). As expected, target genes of Wnt-β-catenin signaling, including Lef1 and c-Myc, decreased following sFRP2 treatment (Figure S11D). Similarly, Irf8 mRNA expression decreased, coincident with an increase in virus NP expression (Figure 6D). Finally, we could show that Irf8 mRNA levels are lower in h2 KO and dKO cells than in WT cells (Figure S11E), that that Irf8 KO cells also show enhanced viral replication (Figure 6E, left panel). We then transduced an empty vector (EV) or Irf8-expressing vector into WT and dKO cells, and subsequently infected them with virus. Compared to EV-transduced cells, Irf8-transduced cells had reduced virus NP mRNA expression following viral infection, in both WT and dKO cells (Figure 6E, right panel). Collectively, these results suggest that HoxC8-C6 enhances viral replication through sFRP2-mediated suppression of β-catenin-Ifr8 signaling (Figure S11F).

Deletion of Suv4-20h2 deteriorates pathology of influenza viral infection in mice

In order to determine the importance of this pathway in a living organism, we examined the effect of Suv4-20hr deficiency on the pathology of influenza viral infection in mice. Since Suv4-20h1−/− mice display perinatal lethality (Schotta et al., 2008), we compared the pathology of influenza infection using macrophage-specific Suv4-20h1 KO (h1 KO^{MC}), Suv4-20h2 KO (h2 KO), and macrophage-specific Suv4-20h1 and Suv4-20h2 double KO (dKO^{MC}) mice, comparing them to WT mice. Importantly, the h2 KO and dKO^{MC}

strains showed reduced survival (Figure 6F), more pathogenic lung histology (Figure 6G) and higher viral replication as assessed by NP mRNA expression in lung, compared to WT or h1 KO^{MC} mice (Figure 6H). Similarly, compared to WT mice, h2 KO mice had impaired respiratory function (e.g., static compliance) (Figure S12A), higher virus titers (Figure S12B) and higher levels of NP mRNA (Figure S12C). Consistent with an enhanced infection, pro-inflammatory cytokine expression was higher in lung tissues (CXCL2, CXCL1) of h2 KO vs WT mice (Figure S12D). Thus, deletion of Suv4-20h2 led to higher rates of viral replication and more severe influenza pathology *in vivo*.

Consistent with our results in MEFs, h2 KO and virus infected-WT mice showed higher levels of HoxC8 and HoxC6 mRNA in lung tissues than uninfected WT mice (Figure 6I). Expression levels of target genes of Wnt-β-catenin signaling, including Lef1 and c-Myc, were reduced in the lung of the virus-infected WT or h2 KO mice (Figure S12E). Similarly, Irf8 mRNA expression was lower in lung tissues obtained from virus-infected h2 KO than WT mice (Figure 6J). Thus, HoxC8-HoxC6 mediated suppression of IFN signaling appears to enhance viral replication in mice lacking the Suv4-20h2 HMT.

Human lung cancer with reduced Suv4-20h2/H4K20me3 and higher HoxC8-C6 levels shows enhanced influenza viral replication

Recent studies have shown that patients with cancer have more severe influenza virus infections and show a higher mortality rate from influenza infection (Kim et al., 2019) (Hermann et al., 2017). The immunocompromised status caused by cancer or its treatment was considered to be the main cause of the more severe influenza pathology. On the other hand, given that the loss of H4K20me3 has been observed in cancer patients (Van Den Broeck et al., 2008), we examined whether decreased levels of H4K20me3 could be correlated with the enhanced severity of influenza in patients with lung cancer. Compared to control tissue, we found that H4K20me3 levels (Figure 7A) and Suv4-20h2 expression (Figure 7B) were both reduced in lung tissues obtained from lung cancer patients with adenocarcinoma (Ad) and squamous cell carcinoma (Sq). In addition, HOXC8 and HOXC6 expression levels were elevated in lung cancer patient tissues (Figure 7C). Using a human normal bronchial epithelial cell line (BEAS-2B) and lung cancer cell line (A549), we found that Suv4-20h2 expression was lower in the lung cancer cell line than in normal bronchial epithelial cells (Figure 7D). Moreover, compared to BEAS-2B, A549 cells also showed increased HoxC8 and HoxC6 expression (Figure 7E), and viral replication was more efficient in A549 vs BEAS-2B cells (Figure 7F). Based on the data presented above, we propose that cancer patients with reduced H4K20me3/Suv4-20h2 and increased HoxC8/HoxC6 expression, which should enhance the influenza replication and account for the more severe pathology observed following influenza infection.

DISCUSSION

The human genome contains over 20,000 genes and a larger number of regulatory elements. Large-scale studies over the last decade have annotated thousands of genes and millions of candidate regulatory elements. In addition, accumulating evidence suggest that chromatin is spatially organized into compartments (e.g., "active" A- and "inactive" B- compartments), TADs, and loops that both reflect and control transcription (Dixon et al., 2012) (Bonev and Cavalli, 2016). In fact, a large number of disease-associated loci map to distal noncoding regions, which potentially are regulatory elements controlling long-range chromatin folding. In the present study, Suv4-20h2 binds the viral protein NP, which results in the inactivation of Suv4-20h2 and the dissociation of cohesin from Suv4-20h2. Inactivation of Suv4-20h2 by viral infection or genetic deletion allows a cohesion-mediated active chromatin loop formation at loci that enhance viral replication. Thus, a chromatin loop formation mediated by interaction of virus protein and Suv4-20h2 appears to contribute to the pathogenesis of influenza viral infection.

CTCF and cohesin are known to be responsible for loop formation (Zuin et al., 2014) (Parelho et al., 2008; Sofueva et al., 2013; Wendt et al., 2008). It has been proposed that cohesin loads at CTCF binding sites (CTCF-BS), resulting in active loop extrusion, while Wapl and its binding partner PDS5 act as cohesin unloading factors (Busslinger et al., 2017; Haarhuis et al., 2017). In the present study, we found that the inactivation of Suv4-20h2 drives cohesin-mediated loop formation, and conversely that Suv4-20h2 inhibits cohesion loading, in a manner most likely independent of Wapl. Similar to a study showing that CTCF partitions the Hox clusters into insulated architectural domains in response to patterning signals during differentiation (Narendra et al., 2015), our data argue that the inactivation of Suv4-20h2 by either influenza viral infection or genetic deletion, regulates loop formation at the HoxC cluster (HoxC8-C6). Thereafter, Polycomb-mediated H3K27me3 and the active H3K27ac mark show a mutually exclusive distribution that establishes the selective expression of HoxC loci. We propose that Suv4-20h2 acts as an alternative cohesin

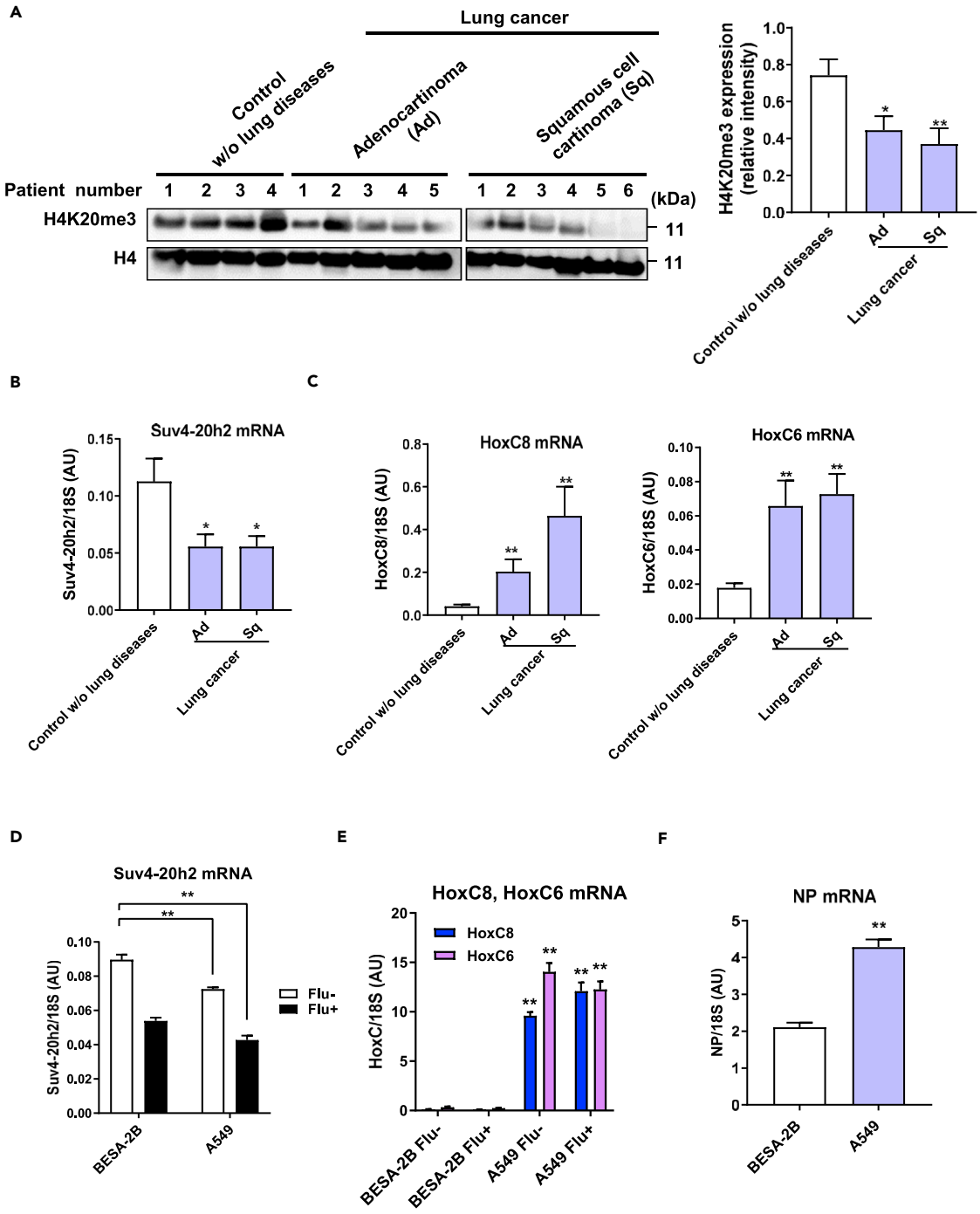

Figure 7. Human lung cancer with reduced Suv4-20h2/H4K20me3 and elevated HoxC8-C6 expression supports enhanced influenza viral replication

(A–D) Histones were extracted from human lung tissues obtained from patients without lung diseases (Control w/o lung disease), or with lung cancer with adenocarcinoma (Ad) or squamous carcinoma (Sq). All were subjected to Western blotting for H4K20me3 and H4 (A, left panel). Protein level was quantified by Western blot densitometry (A, right panel). Data are from four separate experiments. *p< 0.05, **p< 0.01 compared to Control w/o lung disease. Expression levels of Suv4-20h2 (B), HoxC8 and HoxC6 (C) are shown.

(D–F) BEAS-2B and A549 cells were infected with mock (Flu-) or influenza virus (MOI: 0.5; Flu+) for 8 hr mRNA expression of Suv4-20h2 (D), and HoxC8, HoxC6 (E) are shown. **p < 0.01 compared to BEAS-2B, Flu-.mRNA expression of NP is shown (F). **p < 0.01 compared to BEAS-2B.

Data are from three separate experiments. The data in A (right panel)-F are presented as means ± s.e.m. Statistical analysis were carried out using analysis of variance with Bonferroni post t tests for (A–E) and unpaired t test for (F)

unloading factor at specific sites under condition such as influenza virus infection. Exactly how Suv4-20h2 regulates cohesin loading at these sites is not fully understood and will require further study.

Recent studies have shown that patients with lung cancer suffer more severe influenza and COVID-19 infections, and have a higher mortality rate from these viruses (Kim et al., 2019) (Hermann et al., 2017). Whereas an immunocompromised status triggered by cancer or its treatment was thought to be responsible for the severity of the influenza infection, we and others demonstrate that H4K20me3 levels are reduced in breast cancer (Yokoyama et al., 2014), colon cancer (Ozgur et al., 2019) and lung cancer (Figure 7) (Van Den Broeck et al., 2008). Moreover, we have established a link between reduced Suv4-20h2/H4K20me3 and enhanced expression of HoxC6 and HoxC8, which has also been reported for human cancer tissues, such as prostate (Miller et al., 2003), cervical (Alami et al., 1999) and esophageal cancers (Du et al., 2014). We now show that human cancer cells with reduced Suv4-20h2/H4K20me3 levels and elevated HoxC6 and HoxC8 expression, support enhanced viral replication. This indicates that host epigenetic factors may indeed contribute to the severity of respiratory virus infection (e.g. influenza, COVID-19) in patients with cancer.

Limitation of the study

This study focused on chromatin loop formation in the HoxC region in response to influenza virus infection. Genome-wide changes in chromatin 3D structure to viral infection are unknown and require further study. In addition, Suv4-20h2 has been shown to act as an alternative cohesin unloading factor at specific sites under conditions such as influenza virus infection. How Suv4-20h2 regulates cohesin loading at these sites is not exactly understood and requires further study.

STAR★METHODS

Detailed methods are provided in the online version of this paper and include the following:

- KEY RESOURCES TABLE
- RESOURCE AVAILABILITY
  - Lead contact
  - Materials availability
  - Data and code availability
- EXPERIMENTAL MODEL AND SUBJECT DETAILS
  - Mice
- METHOD DETAILS
  - Viruses
  - Virus titer assay
  - Intratracheal influenza viral infection and measurements of respiratory function in mice
  - Histologic analysis and immunohistochemistry of lung tissues
  - Human lung tissue
  - Extraction of core histone proteins
  - H4-tail proteomics
  - Plasmid
  - Retroviral transduction
  - Cell culture
  - Virus infection in cultured cells
  - Nuclear fractionation
  - Immunoprecipitation
  - GSTpull-down assays
  - SILAC labeling, immunoprecipitation and proteomics
  - Immunoprecipitation (IP) and proteomics
  - H4K20me3 activity assay
  - Immunofluorescence (IF)
  - Chromatin immunoprecipitation (ChIP)-qPCR and ChIP-seq
  - 4C-seq library preparation and sequencing
  - Cell sorting
  - DNA fluorescent *in situ* hybridization combined with immunofluorescence
  - Recombinant mouse sFRP2 protein treatment
  - Cell-cycle arrest

- Western blotting
- Quantitative real-time PCR

- QUANTIFICATION AND STATISTICAL ANALYSIS

SUPPLEMENTAL INFORMATION

Supplemental information can be found online at https://doi.org/10.1016/j.isci.2021.102660.

ACKNOWLEDGMENTS

We thank Prof. Susan Gasser and all members of our laboratories for helpful discussion. Y. Imai is partially supported by JSPS, Japan KAKENHI 17H06179, 17K19693, and 15H05978. KS is partially supported by JSPS, Japan KAKENHI 15H05970. TI is partially supported by JSPS, Japan KAKENHI 15H05979. Y. Ichida is partially supported by JSPS, Japan KAKENHI 19K18373.

AUTHOR CONTRIBUTIONS

Y. Imai conceived and supervised the study. M. Shiimori, Y. Ichida, R. Nukiwa, T. Sakuma and H. Abe performed the experiments. M. Shiimori, Y. Ichida, T. Sakuma, H. Abe, R. Kajitani, Y. Fujino, A. Kikuchi, T. Kawamura, T. Kodama, S. Toyooka, K. Shirahige, G. Schotta, K. Kuba, T. Itoh and Y. Imai analyzed the data. Y. Imai wrote the manuscript with input from all authors.

DECLARATION OF INTERESTS

The authors declare no competing interests.

Received: September 22, 2020
Revised: March 20, 2021
Accepted: May 26, 2021
Published: June 25, 2021

REFERENCES

Alami, Y., Castronovo, V., Belotti, D., Flagiello, D., and Clausse, N. (1999). HOXC5 and HOXC8 expression are selectively turned on in human cervical cancer cells compared to normal keratinocytes. Biochem.Biophys.Res. Commun. *257*, 738–745.

Benetti, R., Gonzalo, S., Jaco, I., Schotta, G., Klatt, P., Jenuwein, T., and Blasco, M.A. (2007). Suv4-20h deficiency results in telomere elongation and derepression of telomere recombination. J. Cell Biol. *178*, 925–936.

Bonev, B., and Cavalli, G. (2016). Organization and function of the 3D genome. Nat. Rev. Genet. *17*, 661–678.

Busslinger, G.A., Stocsits, R.R., van der Lelij, P., Axelsson, E., Tedeschi, A., Galjart, N., and Peters, J.M. (2017). Cohesin is positioned in mammalian genomes by transcription, CTCF and Wapl. Nature *544*, 503–507.

Cadigan, K.M., and Waterman, M.L. (2012). TCF/LEFs and Wnt signaling in the nucleus. Cold Spring Harb.Perspect. Biol. *4*, a007906.

Degner, S.C., Wong, T.P., Jankevicius, G., and Feeney, A.J. (2009). Cutting edge: developmental stage-specific recruitment of cohesin to CTCF sites throughout immunoglobulin loci during B lymphocyte development. J. Immunol. *182*, 44–48.

Dekker, J., Belmont, A.S., Guttman, M., Leshyk, V.O., Lis, J.T., Lomvardas, S., Mirny, L.A., O'Shea, C.C., Park, P.J., Ren, B., et al. (2017). The 4D nucleome project. Nature *549*, 219–226.

Subbarao, K., Chen, H., Swayne, D., Mingay, L., Fodor, E., Brownlee, G., Xu, X., Lu, X., Katz, J., Cox, N., and Matsuoka, Y. (2003). Evaluation of a genetically modified reassortant H5N1 influenza A virus vaccine candidate generated by plasmid-based reverse genetics. Virology *305*, 192–200.

Suzuki, A., Obi, K., Urabe, T., Hayakawa, H., Yamada, M., Kaneko, S., Onodera, M., Mizuno, Y., and Mochizuki, H. (2002). Feasibility of ex vivo gene therapy for neurological disorders using the new retroviral vector GCDNsap packaged in the vesicular stomatitis virus G protein. J Neurochem *82*, 953–960.

Van Den Broeck, A., Brambilla, E., Moro-Sibilot, D., Lantuejoul, S., Brambilla, C., Eymin, B., Khochbin, S., and Gazzeri, S. (2008). Loss of histone H4K20 trimethylation occurs in preneoplasia and influences prognosis of non-small cell lung cancer. Clin.Cancer Res. *14*, 7237–7245.

Dixon, J.R., Selvaraj, S., Yue, F., Kim, A., Li, Y., Shen, Y., Hu, M., Liu, J.S., and Ren, B. (2012). Topological domains in mammalian genomes identified by analysis of chromatin interactions. Nature *485*, 376–380.

Du, Y.B., Dong, B., Shen, L.Y., Yan, W.P., Dai, L., Xiong, H.C., Liang, Z., Kang, X.Z., Qin, B., and Chen, K.N. (2014). The survival predictive significance of HOXC6 and HOXC8 in esophageal squamous cell carcinoma. J. Surg. Res. *188*, 442–450.

Fujiwara, S., Hoshizaki, M., Ichida, Y., Lex, D., Kuroda, E., Ishii, K.J., Magi, S., Okada, M., Takao, H., Gandou, M., et al. (2019). Pulmonary phagocyte-derived NPY controls the pathology of severe influenza virus infection. Nat. Microbiol. *4*, 258–268.

Garcia-Robles, I., Akarsu, H., Muller, C.W., Ruigrok, R.W., and Baudin, F. (2005). Interaction of influenza virus proteins with nucleosomes. Virology *332*, 329–336.

Gosgnach, S., Lanuza, G.M., Butt, S.J., Saueressig, H., Zhang, Y., Velasquez, T., Riethmacher, D., Callaway, E.M., Kiehn, O., and Goulding, M. (2006). V1 spinal neurons regulate the speed of vertebrate locomotor outputs. Nature *440*, 215–219.

Guacci, V., Koshland, D., and Strunnikov, A. (1997). A direct link between sister chromatid cohesion and chromosome condensation revealed through the analysis of MCD1 in S. cerevisiae. Cell *91*, 47–57.

Haarhuis, J.H.I., van der Weide, R.H., Blomen, V.A., Yanez-Cuna, J.O., Amendola, M., van Ruiten, M.S., Krijger, P.H.L., Teunissen, H., Medema, R.H., van Steensel, B., et al. (2017). The cohesin release factor WAPL restricts chromatin loop extension. Cell *169*, 693–707 e614.

Hadjur, S., Williams, L.M., Ryan, N.K., Cobb, B.S., Sexton, T., Fraser, P., Fisher, A.G., and Merkenschlager, M. (2009). Cohesins form chromosomal cis-interactions at the developmentally regulated IFNG locus. Nature *460*, 410–413.

Hahn, M., Dambacher, S., Dulev, S., Kuznetsova, A.Y., Eck, S., Worz, S., Sadic, D., Schulte, M., Mallm, J.P., Maiser, A., et al. (2013). Suv4-20h2 mediates chromatin compaction and is important for cohesin recruitment to heterochromatin. Genes Dev. *27*, 859–872.

Hayashi-Takanaka, Y., Maehara, K., Harada, A., Umehara, T., Yokoyama, S., Obuse, C., Ohkawa, Y., Nozaki, N., and Kimura, H. (2015). Distribution of histone H4 modifications as revealed by a panel of specific monoclonal antibodies. Chromosome Res. *23*, 753–766.

Heinz, S., Texari, L., Hayes, M.G.B., Urbanowski, M., Chang, M.W., Givarkes, N., Rialdi, A., White, K.M., Albrecht, R.A., Pache, L., et al. (2018). Transcription elongation can affect genome 3D structure. Cell *174*, 1522–1536 e1522.

Hermann, B., Lehners, N., Brodhun, M., Boden, K., Hochhaus, A., Kochanek, M., Meckel, K., Mayer, K., Rachow, T., Rieger, C., et al. (2017). Influenza virus infections in patients with malignancies – characteristics and outcome of the season 2014/15. A survey conducted by the Infectious Diseases Working Party (AGIHO) of the German Society of Haematology and Medical Oncology (DGHO). Eur. J. Clin. Microbiol. Infect. Dis. *36*, 565–573.

Hillesheim, A., Nordhoff, C., Boergeling, Y., Ludwig, S., and Wixler, V. (2014). beta-catenin promotes the type I IFN synthesis and the IFN-dependent signaling response but is suppressed by influenza A virus-induced RIG-I/NF-kappaB signaling. Cell Commun.Signal. *12*, *29*.

Hou, C., Dale, R., and Dean, A. (2010). Cell type specificity of chromatin organization mediated by CTCF and cohesin. Proc. Natl. Acad. Sci. U S A *107*, 3651–3656.

Jorgensen, S., Schotta, G., and Sorensen, C.S. (2013). Histone H4 lysine 20 methylation: key player in epigenetic regulation of genomic integrity. Nucleic Acids Res. *41*, 2797–2806.

Kaur, A., Webster, M.R., Marchbank, K., Behera, R., Ndoye, A., Kugel, C.H., 3rd, Dang, V.M., Appleton, J., O'Connell, M.P., Cheng, P., et al. (2016). sFRP2 in the aged microenvironment drives melanoma metastasis and therapy resistance. Nature *532*, 250–254.

Kim, Y.J., Lee, E.S., and Lee, Y.S. (2019). High mortality from viral pneumonia in patients with cancer. Infect Dis. *51*, 502–509.

Klaus, A., and Birchmeier, W. (2008). Wnt signalling and its impact on development and cancer. Nat. Rev. Cancer *8*, 387–398.

Langmead, B., and Salzberg, S.L. (2012). Fast gapped-read alignment with Bowtie 2. Nat. Methods *9*, 357–359.

Lei, H., Wang, H., Juan, A.H., and Ruddle, F.H. (2005). The identification of Hoxc8 target genes. Proc. Natl. Acad. Sci. U S A *102*, 2420–2424.

Lei, H., Juan, A.H., Kim, M.S., and Ruddle, F.H. (2006). Identification of a Hoxc8-regulated transcriptional network in mouse embryo fibroblast cells. Proc. Natl. Acad. Sci. U S A *103*, 10305–10309.

Lesbats, P., Engelman, A.N., and Cherepanov, P. (2016). Retroviral DNA integration. Chem. Rev. *116*, 12730–12757.

Li, H., Handsaker, B., Wysoker, A., Fennell, T., Ruan, J., Homer, N., Marth, G., Abecasis, G., Durbin, R., and Genome Project Data Processing, S. (2009). The sequence alignment/map format and SAMtools. Bioinformatics *25*, 2078–2079.

Miller, G.J., Miller, H.L., van Bokhoven, A., Lambert, J.R., Werahera, P.N., Schirripa, O., Lucia, M.S., and Nordeen, S.K. (2003). Aberrant HOXC expression accompanies the malignant phenotype in human prostate. Cancer Res. *63*, 5879–5888.

Morita, M., Kuba, K., Ichikawa, A., Nakayama, M., Katahira, J., Iwamoto, R., Watanebe, T., Sakabe, S., Daidoji, T., Nakamura, S., et al. (2013). The lipid mediator protectin D1 inhibits influenza virus replication and improves severe influenza. Cell *153*, 112–125.

Narendra, V., Rocha, P.P., An, D., Raviram, R., Skok, J.A., Mazzoni, E.O., and Reinberg, D. (2015). CTCF establishes discrete functional chromatin domains at the Hox clusters during differentiation. Science *347*, 1017–1021.

Nativio, R., Wendt, K.S., Ito, Y., Huddleston, J.E., Uribe-Lewis, S., Woodfine, K., Krueger, C., Reik, W., Peters, J.M., and Murrell, A. (2009). Cohesin is required for higher-order chromatin conformation at the imprinted IGF2-H19 locus. PLoS Genet. *5*, e1000739.

Nelson, D.M., Jaber-Hijazi, F., Cole, J.J., Robertson, N.A., Pawlikowski, J.S., Norris, K.T., Criscione, S.W., Pchelintsev, N.A., Piscitello, D., Stong, N., et al. (2016). Mapping H4K20me3 onto the chromatin landscape of senescent cells indicates a function in control of cell senescence and tumor suppression through preservation of genetic and epigenetic stability. Genome Biol. *17*, 158.

Ozgur, E., Keskin, M., Yoruker, E.E., Holdenrieder, S., and Gezer, U. (2019). Plasma histone H4 and H4K20 trimethylation levels differ between colon cancer and precancerous polyps. In Vivo *33*, 1653–1658.

Parelho, V., Hadjur, S., Spivakov, M., Leleu, M., Sauer, S., Gregson, H.C., Jarmuz, A., Canzonetta, C., Webster, Z., Nesterova, T., et al. (2008). Cohesins functionally associate with CTCF on mammalian chromosome arms. Cell *132*, 422–433.

Scheller, M., Schonheit, J., Zimmermann, K., Leser, U., Rosenbauer, F., and Leutz, A. (2013). Cross talk between Wnt/beta-catenin and Irf8 in leukemia progression and drug resistance. J. Exp. Med. *210*, 2239–2256.

Schotta, G., Sengupta, R., Kubicek, S., Malin, S., Kauer, M., Callen, E., Celeste, A., Pagani, M., Opravil, S., De La Rosa-Velazquez, I.A., et al. (2008). A chromatin-wide transition to H4K20 monomethylation impairs genome integrity and programmed DNA rearrangements in the mouse. Genes Dev. *22*, 2048–2061.

Schwarzer, W., Abdennur, N., Goloborodko, A., Pekowska, A., Fudenberg, G., Loe-Mie, Y., Fonseca, N.A., Huber, W., Haering, C.H., Mirny, L., et al. (2017). Two independent modes of chromatin organization revealed by cohesin removal. Nature *551*, 51–56.

Sofueva, S., Yaffe, E., Chan, W.C., Georgopoulou, D., Vietri Rudan, M., Mira-Bontenbal, H., Pollard, S.M., Schroth, G.P., Tanay, A., and Hadjur, S. (2013). Cohesin-mediated interactions organize chromosomal domain architecture. EMBO J. *32*, 3119–3129.

Solovei, I., and Cremer, M. (2010). 3D-FISH on cultured cells combined with immunostaining. Methods Mol. Biol. *659*, 117–126.

Wang, X., Xu, M., Zhao, G., Liu, G., Hao, D., Lv, X., and Liu, D. (2015). Exploring CTCF and cohesin related chromatin architecture at HOXA gene cluster in primary human fibroblasts. Sci. China Life Sci. *58*, 860–866.

Watanabe, T., Watanabe, S., and Kawaoka, Y. (2010). Cellular networks involved in the influenza virus life cycle. Cell Host Microbe *7*, 427–439.

Wendt, K.S., and Peters, J.M. (2009). How cohesin and CTCF cooperate in regulating gene expression. Chromosome Res. *17*, 201–214.

Wendt, K.S., Yoshida, K., Itoh, T., Bando, M., Koch, B., Schirghuber, E., Tsutsumi, S., Nagae, G., Ishihara, K., Mishiro, T., et al. (2008). Cohesin mediates transcriptional insulation by CCCTC-binding factor. Nature *451*, 796–801.

West, M.J. (2017). Chromatin reorganisation in Epstein-Barr virus-infected cells and its role in cancer development. Curr.Opin.Virol. *26*, 149–155.

Xia, Y., Jin, R., Zhao, J., Li, W., and Shen, H. (2020). Risk of COVID-19 for patients with cancer. Lancet Oncol. *21*, e180.

Yamamoto, K., Chikaoka, Y., Hayashi, G., Sakamoto, R., Yamamoto, R., Sugiyama, A., Kodama, T., Okamoto, A., and Kawamura, T. (2015). Middle-down and chemical proteomic approaches to reveal histone H4 modification dynamics in cell cycle: label-free semi-quantification of histone tail peptide modifications including phosphorylation and highly sensitive capture of histone PTM binding proteins using photo-reactive crosslinkers. Mass Spectrom. *4*, A0039.

Yokoyama, Y., Matsumoto, A., Hieda, M., Shinchi, Y., Ogihara, E., Hamada, M., Nishioka, Y., Kimura, H., Yoshidome, K., Tsujimoto, M., et al. (2014). Loss of histone H4K20 trimethylation predicts poor prognosis in breast cancer and is associated with invasive activity. Breast Cancer Res. *16*, R66.

Zhang, Y., Liu, T., Meyer, C.A., Eeckhoute, J., Johnson, D.S., Bernstein, B.E., Nusbaum, C., Myers, R.M., Brown, M., Li, W., et al. (2008). Model-based analysis of ChIP-seq (MACS). Genome Biol. *9*, R137.

Zuin, J., Dixon, J.R., van der Reijden, M.I., Ye, Z., Kolovos, P., Brouwer, R.W., van de Corput, M.P., van de Werken, H.J., Knoch, T.A., van, I.W.F., et al. (2014). Cohesin and CTCF differentially affect chromatin architecture and gene expression in human cells. Proc. Natl. Acad. Sci. U S A *111*, 996–1001.

STAR★METHODS

KEY RESOURCES TABLE

REAGENT or RESOURCE	SOURCE	IDENTIFIER
Antibodies		
Anti-GFP	Abcam	Cat# ab5450; RRID:AB_304897
Anti-NUP153	Abcam	Cat# ab24700; RRID:AB_2154467
Anti-NUP98	Abcam	Cat# ab50610; RRID:AB_881769
Anti-SUV420h1	Abcam	Cat# ab118659; RRID:AB_10899963
Anti-SUV420h2	Abcam	Cat# ab91224; RRID:AB_2050349
Anti-H3K27acetylation	Abcam	Cat# ab4729; RRID:AB_2118291
Anti-Histone H4	Abcam	Cat# ab10158; RRID:AB_296888
Anti-Rad21	Abcam	Cat# ab992; RRID:AB_2176601
Anti-LaminB1	Abcam	Cat# ab16048; RRID:AB_443298
Anti-SFRP2	Abcam	Cat# ab86379; RRID:AB_1925427
Anti-Influenza A Virus Nucleoprotein	Abcam	Cat# ab128193; RRID:AB_11143769
Anti-WAPL	Abcam	Cat# ab70741; RRID:AB_2216719
Anti-Pds5b	Abcam	Cat# ab70298; RRID:AB_1269710
Anti-TBP	Abcam	Cat# ab51841; RRID:AB_945758
Anti-SMC1	Active motif	Cat# 61067; RRID:AB_2688006
Anti-SMC3	Abcam	Cat# ab9263; RRID:AB_307122
Anti-AM-tag	Active motif	Cat# 91111; RRID:AB_2793779
Anti-FLAG M2	SIGMA	Cat# F1804; RRID:AB_262044
Anti-H3K9 trimethylation	Active motif	Cat# 39161; RRID:AB_2532132
Anti-NUP62	BD Biosciences	Cat# 610497; RRID:AB_397863
Anti-GAPDH	Cell signaling Technology	Cat# 2118; RRID:AB_561053
Anti-Ezh2	Cell signaling Technology	Cat# 5246; RRID:AB_10694683
Anti-active β-Catenin	Cell signaling Technology	Cat# 8814; RRID:AB_11127203
Anti-NIPBL	Santa Cruz Biotechnology	Cat# sc-374625; RRID:AB_10989775
Anti-Influenza A Virus PB2	GeneTex	Cat# GTX125925; RRID:AB_11170601
Anti-Influenza A Virus M1	GeneTex	Cat# GTX127356; RRID:AB_2885647
Anti-HP1alpha	MBL	Cat# BMP001; RRID:AB_842932
Anti-HP1beta	MBL	Cat# BMP002; RRID:AB_843158
Anti-HP1gamma	MBL	Cat# BMP003; RRID:AB_843159
Anti-H3K27 trimethylation	Millipore	Cat# 07-449; RRID:AB_310624
Anti-CTCF	Millipore	Cat# 07-729; RRID:AB_441965
Normal mouse IgG	Millipore	Cat# 12-371; RRID:AB_145840
Normal rabbit IgG	Millipore	Cat# 12-370; RRID:AB_145841
Anti-H4K20 monomethylation	(Hayashi-Takanaka et al., 2015)	N/A
Anti-H4K20 dimethylation	(Hayashi-Takanaka et al., 2015)	N/A
Anti-H4K20 trimethylation	Abcam	Cat# ab9053; RRID:AB_306969
Anti-H4K20 trimethylation	Active motif	Cat# 39671; RRID:AB_2650526
Anti-HOXC8	Proteintech	Cat# 15448-1-AP; RRID:AB_2878140
Alexa Fluor 488 donkey mouse IgG antibody	Thermo Fisher Scientific	Cat# A-21202; RRID:AB_141607
Alexa Fluor 488 donkey rabbit IgG antibody	Thermo Fisher Scientific	Cat# A-21206; RRID:AB_2535792

(*Continued on next page*)

Continued

REAGENT or RESOURCE	SOURCE	IDENTIFIER
Alexa Fluor 488 donkey goat IgG antibody	Thermo Fisher Scientific	Cat# A-11055; RRID:AB_2534102
Alexa Fluor 488 goat rat IgG antibody	Thermo Fisher Scientific	Cat# A-11006; RRID:AB_2534074
Alexa Fluor 555 donkey mouse IgG antibody	Thermo Fisher Scientific	Cat# A-31570; RRID:AB_2536180
Alexa Fluor 555 donkey rabbit IgG antibody	Thermo Fisher Scientific	Cat# A-31572; RRID:AB_162543
Bacterial and virus strains		
A/Puerto Rico/8/34 (H1N1; PR8) influenza virus	(Subbarao et al., 2003)	N/A
Escherichia coli BL21	Takara	9126
Escherichia coli DH5α	Nippon gene	316-06233
Biological samples		
Patient lung tissue	Okayama University biobank	http://biobank.ccsv.okayama-u.ac.jp/
Chemicals, peptides, and recombinant proteins		
NotI	NEB	R3189L
XhoI	Takara	1094A
EcoRI	NEB	R3101L
XbaI	Takara	1093A
DMEM	Sigma	D5796
DMEM	Thermo Fisher Scientific	11054001
Sodium pyruvate	Thermo Fisher Scientific	11360-070
Fetal bovine serum	CCB	171012
β-mercaptoethanol	Invitrogen	123521985023
MEM-NEAA	Thermo Fisher Scientific	11140-050
ESGRO Mouse LIF Medium Supplement	Millipore	ESG1107
BEGM Bullet kit	Lonza	CC-3170
Lipofectamine 3000 Transfection Reagent	Thermo Fisher Scientific	L3000-015
Ficoll	GE Healthcare	17144002
Protease inhibitor (Complete, Mini, EDTA-free)	Roche	04 693 159 001
Benzonase	Sigma	70746-3CN
RNase inhibitor	TOYOBO	SIN-201X5
Dynabeads protein G	Invitrogen	DB10004
3XFLAG peptide	Sigma	F4799-4MG
IPTG	Wako	096-05143
Glutathione sepharise 4B	GE healthcare	17075601
PreScission protease	GE healthcare	27084301
Sera-Mag beads	Cytiva	17152104010150
Influenza A H1N1 Nucleoprotein/NP Protein	SinoBiological	11675-V08B
Influenza A H1N1Matrix protein 1/ M1 Protein	SinoBiological	40010-V07E
Recombinant SUV420H2 (2-281) protein	Active motif	31466
Recombinant Polynucleosomes (H3.1)	Active motif	81014
Mouse Cot-1 DNA	Invitrogen	18440-016
Salmon-sperm DNA	Invitrogen	15632011
Recombinant mouse sFRP2 protein	R&D systems	1169-FR-025
Thymidine	Sigma	T1895
Nitrocellulose membrane	Thermo Fisher Scientific	LC200
LDS buffer	Thermo Fisher Scientific	NP0007
ECL prime western blot detection reagent	GE Healthcare	RPN2232

(*Continued on next page*)

Continued

REAGENT or RESOURCE	SOURCE	IDENTIFIER
Critical commercial assays		
Histone purification mini kit	Active motif	40026
In-Fusion HD Cloning Kit	Takara	Z9648N
Subcellular protein fractionation kit	Thermo Fisher Scientific	78840
SILAC protein quantification Kit	Thermo Fisher Scientific	A33969
ChIP-IT express kit	Active motif	53008
PCR purification kit	Qiagen	28104
Cut&Tag-IT kit	Active motif	53160
FISH Tag DNA Kit	Invitrogen life technologies	F32951
Cytoplasmic and nuclear fractionation kit	Thermo Fisher Scientific	78833
RNeasy mini kit	QIAGEN	74104
Primescript RT reagent kit	Takara	RR037B
Deposited data		
ChIP-seq	This paper	SRA: PRJNA727026
Proteomics	This paper	PRIDE: PXD025676
Experimental models: cell lines		
MDCK	ATCC	CCL-34
MEF WT	Hahn et al., 2013	N/A
MEF Suv420h1 KO	Hahn et al., 2013	N/A
MEF Suv420h2 KO	Hahn et al., 2013	N/A
MEF Suv420h1h2 double KO	Hahn et al., 2013	N/A
ES ES129B6C4	Hahn et al., 2013	N/A
ES SW26	Hahn et al., 2013	N/A
Mouse ES Suv420h2-HA-FLAG KI	Hahn et al., 2013	N/A
Mouse ES Suv420h2-GFP KI	Hahn et al., 2013	N/A
293T	ATCC	CRL-3216
293FT	Thermo Fisher Scientific	R70007
293GP2	Takara	631458
A549	ATCC	CL-185
BEAS-2B	ATCC	CRL-9609
Experimental models: organisms/strains		
Mouse/Suv-4-20h2 KO	Schotta et al., 2008	N/A
Mouse/Suv4-20h1-floxed	Schotta et al., 2008	N/A
Mouse/ macrophage-specific Suv4-20h1 KO	This paper	N/A
Mouse/ macrophage-specific Suv4-20h1 and Suv-4-20h2 double KOs	This paper	N/A
Oligonucleotides		
Sequence of oligonucleotides in this paper	This paper	Table S1
Recombinant DNA		
pEGFP	Chlontech	6080-1
pEF4	Thermo Fisher Scientific	V94220
pGEX6P1	Amersham	27-4597-01
pAM_1C	Active motif	53023
pGCDN-IRES/EGFP	(Suzuki et al., 2002)	N/A

(*Continued on next page*)

Continued

REAGENT or RESOURCE	SOURCE	IDENTIFIER
pEGFP-Suv420h2 FL	This paper	N/A
pEGFP-Suv420h2 SET	This paper	N/A
pEGFP-Suv420h2 Clamp	This paper	N/A
pEF4-Suv420h2 FL	This paper	N/A
pEF4-Suv420h2 SET	This paper	N/A
pEF4-Suv420h2 Clamp	This paper	N/A
pGEX6P1-Suv420h2 FL	This paper	N/A
pGEX6P1-Suv420h2 SET	This paper	N/A
pGEX6P1-Suv420h2 Clamp	This paper	N/A
pAM_1C-Suv420h2	This paper	N/A
pGCDN-IRES/EGFP-Suv420h2-AM-tag	This paper	N/A
pEF4-HP1α	This paper	N/A
pGEX6P1-HP1α	This paper	N/A
pGEX6P1-PR8-PB2	This paper	N/A
pGEX6P1-PR8-NP	This paper	N/A
pGEX6P1-PR8-M1	This paper	N/A
pGEX6P1-PR8-NS1	This paper	N/A
pEGFPp-HoxC8	This paper	N/A
pGEX6P1-GFP-HoxC8	This paper	N/A
BAC clone B6Ng01-350C10	RIKEN BRC	B6Ng01-350C10
BAC clone B6Ng01-237E10	RIKEN BRC	B6Ng01-237E10
Software and algorithms		
Progenesis QI software	Nonlinear Dynamics Ltd	https://www.nonlinear.com/progenesis/qi/
MASCOT	Matrix Science Ltd	https://www.matrixscience.com/
Bowtie2	(Langmead and Salzberg, 2012)	http://bowtie-bio.sourceforge.net/bowtie2/index.shtml
SAMtools	(Li et al., 2009)	http://samtools.sourceforge.net/
MACS2	Zhang et al., 2008	https://pypi.org/project/MACS2/
Nikon NIS-Elements AR Analysis	Nikon	https://www.microscope.healthcare.nikon.com/ja_JP/products/software/nis-elements/nis-elements-advanced-research
GraphPad Prism	GraphPad	https://www.graphpad.com/scientific-software/prism/

RESOURCE AVAILABILITY

Lead contact

Further information and requests for resources and reagents should be directed to and will be fulfilled by the lead contact, Yumiko Imai (y-imai@nibiohn.go.jp).

Materials availability

Reagents generated in this study are available upon request.

Data and code availability

Data generated in this study are available in SRA under the accession numbers PRJNA727026 for ChIP-seq data. Proteomics data are available in PRIDE under the accession numberPXD025676. All Software packages and methods used in this study are referenced under Method Details.

EXPERIMENTAL MODEL AND SUBJECT DETAILS

Mice

Suv4-20h2 KO and Suv4-20h1-floxed mice were provided by Dr. Gunnar Schotta (Schotta et al., 2008). Suv4-20h1-floxed mice were crossed with Lysozyme Cre recombinase strain to generate macrophage-specific Suv4-20h1 KO mice. Macrophage-specific Suv4-20h1 KO mice were further crossed with Suv4-20h2 KO mice to generate macrophage-specific Suv4-20h1 and Suv4-20h2 double KOs mice. Only sex- and age-matched mice were used for the experiment. Mice were housed in specific pathogen-free conditions in accordance with Institutional guidelines. All animal procedures were performed according to the protocols provided by the Institutional Animal Care and Use Committee of the National Institutes of Biomedical Innovation, Health and Nutrition.

METHOD DETAILS

Viruses

A/Puerto Rico/8/34 (H1N1; PR8) influenza virus was grown in the allantoic cavities of 11-day-old embryonated chicken eggs. All infection experiments were performed according to the guide provided by the Biosafety Committee of the National Institutes of Biomedical Innovation, Health and Nutrition and performed under Biosafety Level 2 (BSL2) condition.

Virus titer assay

Focus forming unit (FFU) assay was performed as we described previously (Morita et al., 2013) (Fujiwara et al., 2019). In brief, MDCK cells were plated at 2×10^4 cells/well of a 96-well plate. At 24 hrs after infection with serially diluted supernatants or tissue lysates containing virus, the cells were fixed with paraformaldehyde in PBS containing 0.1% Triton X-100. Anti-influenza virus nucleoprotein (NP) antibodies (Abcam) were used as primary antibodies to detect viral antigens. Antibody binding to viral proteins was detected with an Alexa Fluor 488-conjugated secondary antibody (Thermo Fisher Scientific).

Intratracheal influenza viral infection and measurements of respiratory function in mice

Mice were intratracheally infected with influenza viruses, as we described previously (Morita et al., 2013) (Fujiwara et al., 2019). In brief, mice were anesthetized by intraperitoneal injection of ketamin (75 mg/kg) and xylazine (20 mg/kg). A 24-gauge catheter was inserted into the trachea and mice received either a suspension of influenza viruses (PR8) in 50 μl of PBS or the same volume of PBS vehicle. Mice were monitored and weighed daily post infection. For respiratory function, static compliance was measure using the flexiVent system (SCIREQ).

Histologic analysis and immunohistochemistry of lung tissues

Lung tissue was fixed in 10% buffered formalin and processed for histologic analysis (H&E) and immunohistochemistry.

Human lung tissue

Lung tissues obtained from patients without lung diseases (control), and lung cancer with adenocarcinoma (Ad) or squamous cell carcinoma (Sq), were provided by the Biobank of the Okayama University Hospital.

Extraction of core histone proteins

Core histone proteins from lung tissues or MEFs were extracted by using the histone purification mini kit (Active motif). Extracted histone core proteins were further precipitated with 4% perchloric acid overnight at 4°C and washed twice with acetone containing 0.2% HCl, followed by acetone wash twice. The pellet was resuspended in sterile water and subjected to Western blotting analysis and/or H4-tail proteomics analysis.

H4-tail proteomics

The detailed methods were previously described (Yamamoto et al., 2015). In brief, extracted histones were digested with AspN endoproteinase, separated with C18 column, fragmented with electron transfer dissociation, and measured with Orbitrap Elite (Thermo Fisher Scientific). MS and retention time of precursor ions were aligned and the areas under the curve (AUC) of their intensities were calculated with Progenesis QI software version 2.0 (Nonlinear Dynamics Ltd.). MS/MS spectra were searched with MASCOT software version 2.5 (Matrix Science Ltd.) to identify peptide and localize the PTMs. Abundances of each K20

methylation states were reconstituted by adding the AUC of precursor ions that contain each K20 methylation state, namely K20me0, K20me1, K20me2, and K20me3.

Plasmid

Coding sequences of mouse full length Suv420h2, or of the SET domain, or clamp domain of Suv420h2 were cloned into pEGFP (addgene), pEF4 (Invitrogen), and pGEX6P1 vectors in order to generate GFP-tagged, FLAG-tagged full length, SET domain, or clamp domain versions of Suv420h2, respectively. Also, full length of Suv420h2 was cloned into pAM_1C vector (Active motif) by In-Fusion HD Cloning kit (Takara) and then AM-tagged Suv420h2 full length was cloned into pGCDN-IRES/EGFP retroviral vector by using restriction enzyme site of NotI and XhoI. For HP1α, cording sequence of mouse HP1α was cloned into pEF4 vector by using restriction enzyme site of EcoRI and XbaI. pGEX6P1 HP1α was generated by In-Fusion HD Cloning kit (Takara). Other pGEX6P1 constructs including pGEX6P1 PR8-PB2, pGEX6P1 PR8-NP, pGEX6P1 PR8-M1, and pGEX6P1 PR8-NS1 as well as GFP-tagged HoxC8 (pEGFP+HoxC8) were generated by In-Fusion HD Cloning kit (Takara). Primer sequences used for all cloning constructs were listed in Table S1.

Retroviral transduction

Constructed retroviral vectors expressing Suv4-20h2 full length, deletion mutants (SET domain or Clamp domain), or IRF8 were converted to the corresponding retroviruses packaged in VSV-G envelop by transfecting the vectors into 293GP2 cells. The resultant retroviruses were then transduced to the WT or dKO MEF cells with 4 μg/mL of polybrene by spinoculation of 1,000 *g* for 1 hr at 32°C. Suv4-20h2 full length or deletion mutants transduced cells were plated onto 96 well plate (0.8 cell/well) and cultured. After 2 weeks, each single clone was isolated.

Cell culture

Immortalized mouse embryonic fibroblast (MEF) cells were cultured in high glucose DMEM (Sigma) with L-Glutamine complemented supplemented with sodium pyruvate, 10% fetal bovine serum (FBS), β-mercaptoethanol, and MEM Non-Essential Amino Acids solution (NEAA) (Thermo Fisher Scientific) in a 37°C incubator at 5% of CO_2. ES cells were maintained in DMEM (Thermo Fisher Scientific) with NEAA, L-glutamine, β-mercaptoethanol, 15% FBS, and ESGRO Mouse LIF Medium Supplement (Millipore). 293T cells, 293FT cells, 293GP2, and A549 cells were cultured in DMEM supplemented with 10% fetal bovine serum. BEAS-2B (human bronchial epithelial cells) cells were cultured in BEGM Bullet Kit (Lonza).

Virus infection in cultured cells

For influenza virus infection, cells on culture plates were infected with influenza virus (H1N1; PR8) at the indicated multiplicity of infection (MOIs) in DMEM without FBS for 60 min at 37°C. Cells were washed and incubated in DMEM supplemented with 10% FBS for the indicated time periods, and the supernatants and cell pellet were collected for the subsequent analysis.

Nuclear fractionation

Nuclei of the cells were isolated by spinning through a Ficoll gradient, as we previously described (Hahn et al., 2013). In brief, cells were harvested by trypsinization, washed twice in 10 mL PBS, and resuspended in 1 mL DMEM (Sigma). Cell suspension was gently overlayed on 2mL of NI-buffer (1.6 mL of NI-stock which is composed of 100 mM Tris-HCl pH 7.4, 10 mM $MgCl_2$, 10 mM $CaCl_2$, 2% of NP40 and 1.6% of Triton X-100, 0.4 mL of Ficoll, and 2 μL of DMSO). Cells were centrifuged with increasing speeds from 400 rpm to 800 rpm (30s/400 rpm, 30s/500 rpm, 30s/600 rpm, 30s/700 rpm, and 6 min/800 rpm). The pellet was washed with 1mL of cold PBS, and centrifuged at 800 rpm for 5 min at 4°C. For further nuclear fractionation, pellet of the nuclear fraction isolated as described above, was resuspended in low salt buffer (50 mM Tris-HCl pH 7.5, 150 mM KCl, 1 mM EDTA, 20% glycerol, 0.1% NP, Protease inhibitor (Roche) and incubated at 37°C with benzonase (Merck Millipore) for 15 min, followed by mild sonication in BioRuptor (Cosmo Bio). After centrifugation at 13,000 rpm for 10 min at 4°C, soluble nuclear fraction was collected as Fraction I. The protein pellet was further resuspended in high salt buffer (50mM Tris-HCl pH 7.5, 500mM KCl, 1mM EDTA, 20% glycerol, 0.1% NP, Protease inhibitor (Roche)) and kept on ice for 30 min. The pellet was then sonicated in BioRuptor on high for 15 min (repeating cycles of a sonication for 30 s and interval for 60 s). They were centrifuged for 10 min at 13,000 rpm at 4°C and saved as Fraction II. The individual fraction was resuspended in RIPA buffer (50mM Tris-HCl pH8.3, 150mM NaCl, 1mM EDTA, 1% NP40, 0.25% sodium deoxycholate, proteinase inhibitor (Roche)) for further immunoprepicitation and Western blot analysis. In

some experiments, cytoplasmic and nuclear fraction of the cells were segregated by Subcellular protein fractionation kit (Thermo Scientific) in the presence of protease inhibitor (Roche) and 1 U/ml of RNase inhibitor (Toyobo), and each fraction was proceeded for Western blot analysis.

Immunoprecipitation

Nuclei of WT and Suv4-20h2$^{HA-Flag}$ mES cells were isolated by spinning through a Ficoll gradient, and used for immunoprecipitation with Flag antibody (Sigma). In brief, nuclear lysates were incubated with 5μg of Flag M2 antibody (Sigma) or normal mouse IgG (Millipore) overnight at 4°C on a rotating wheel. Then they were incubated with 25μL of Dynabeads protein G (Thermo Fisher Scientific) for 1 hr at 4°C. The beads were washed five times with PBS, and eluted with 3×FLAG peptide (Sigma) in TSB (50 mM Tris-HCl pH 7.4, 150 mM NaCl). Proteins were separated on SDS-PAGE and analyzed by Western blot.

GSTpull-down assays

GST fusion proteins were expressed from pGEX6P1 vector in BL21 competent cells. For purification of GST-tagged proteins, bacterial culture was first grown at 37°C until OD600 reaches ~0.6, and protein expression was induced by 0.2mM of IPTG. After bacterial pellet was centrifuged at 6,000 ×g for 15 min at 4°C, they were resuspended in cold PBS in the presence of protease inhibitor (Roche) and homogenized with Bio-Ruptor for 15 min (repeating cycles of a sonication for 30 s and interval for 60 s) on ice. They were then treated with 1% Triton X-100 for 30 min at 4°C in a rotator wheel. Bacterial pellet was centrifuged at 5,000 ×g for 30 min at 4°C, and supernatants were transferred to GraviTrap (GE Healthcare) and GST-tagged protein was purified. Protein expression was confirmed by Coomassie blue staining, and concentration was determined by nanodrop. GST-tagged proteins were incubated with precleared nuclear lysates of ES Suv420h2-FLAG. 50 μg of each GST-fusion protein and 200 μg of ES cell lysates either uninfected or infected with influenza virus were incubated at 4°C overnight. Glutathione Sepharose 4B (GE Healthcare) was added to the mixture and rotated overnight at 4°C. They were centrifuged at 500×g for 5 min at 4°C and washed twice with PBS. After cleavage with PreScission protease (GE Healthcare) at 4°C overnight, they were subjected to Western blot analysis.

SILAC labeling, immunoprecipitation and proteomics

Suv4-20h2^{AM-Tag} MEF cells were cultured in labeling media using SILAC protein Quantitation Kit (Thermo Fisher Scientific) containing heavy isotope ($^{13}C_6$ L-Lysine-2HCL) or light isotope (L-Lysine-2HCL) at least ten cell divisions. The medium also contained 10% dialyzed serum. For immunoprecipitation, nuclei of Suv4-20h2^{AM-Tag} MEF cells were isolated by spinning through a Ficoll gradient, and used for IP with AM-Tag Ab. In brief, nuclear lysates were incubated with 5 μg of AM-Tag antibody (Active motif) or normal mouse IgG (Millipore) overnight at 4°C on a rotating wheel. Then they were incubated with 25 μL of Dynabeads protein G (Thermo Fisher Scientific) for 1 hr at 4°C. The beads were washed five times with PBS and eluted with LDS buffer (Thermo Fisher Scientific) Proteins were separated on SDS-PAGE and stained by CBB. Proteins were subjected to proteomics analysis in our facility.

Immunoprecipitation (IP) and proteomics

Nuclei of Suv4-20h2^{AM-Tag} MEF cells were isolated by spinning through a Ficoll gradient, and used for IP with AM-Tag antibody (Active motif). Then they were incubated with 5 μL of Sera-Mag beads (Cytiva) for 1 hr at 4°C. The beads were washed five times with PBS and eluted with elution buffer (50 mM Tris-HCl pH7.5) Proteins were subjected to proteomics analysis by Kazusa DNA Research Institute.

H4K20me3 activity assay

Human SET domain of SUV4-20h2 (2-281) (Active motif) was pre-incubated with virus NP or M1 protein (SinoBiological) (0, 0.05, 0.5, or 1.0 μg) at room temperature for 1 hr and then incubated with polynucleosomes (Active motif) (1.0 μg) for additional 3 hr. Protein samples were subjected to Western blot analysis using specific antibodies.

Immunofluorescence (IF)

For IF analyses, cells were fixed with 4% paraformaldehyde and were permeabilized in 0.1% Triton X-100 and were blocked in blocking buffer (PBS, 2.5% BSA, 0.1% Tween 20. The cells were incubated with the following primary antibodies: H4K20me1, H4K20me2, H4K20me3 and appropriate secondary antibodies (Table S2). Cover slips were mounted with mounting medium containing Hoechst. Images were analyzed

with a multiphoton laser microscope (A1R MP, Nikon) or a confocal laser scanning microscope (A1 HD25, Nikon). Acquired images were analyzed with NIS-Elements AR Analysis software (Nikon).

Chromatin immunoprecipitation (ChIP)-qPCR and ChIP-seq

ChIP assay was performed by using a ChIP-IT express kit (Active motif). Cells were fixed in 1% formaldehyde, and chromatin was sheared using a Picoruptor (Diagenode) to an average of 200–600 bp of fragments. For each reaction, 25 μg of sheared chromatin were incubated with 5μg antibodies overnight at 4°C. Precipitated DNA was purified using PCR purification kit (Qiagen) and subjected to qPCR and/or ChIP-sequencing. Antibodies used for ChIP analysis and primers used for ChIP-qPCR were summarized in Table S2 and S1, respectively.

4C-seq library preparation and sequencing

5× 10^6 cells were crosslinked with 1% formaldehyde at room temperature for 10 min, quenched with 2 M glycine for 10 min, and washed with phosphate-buffered saline. The crosslinked cells were incubated in lysis buffer (50 mM Tris-HCl pH 7.5, 150 mM NaCl, 5 mM EDTA, 0.5% NP-40, 1% Triton X-100, and protease inhibitor) for 1 hr on ice. After being centrifuged at 800×g for 5 min at 4°C, the supernatants were removed. The cell pellets were resuspended in 0.5% SDS solution and incubated for 10 min at 62°C. To quench the SDS, 10% Triton X-100 was then added per sample. And, the samples were digested in 1× buffer B with 30 U *CSP6I* (Thermo fisher scientific) at 37°C overnight with continuous agitation (900 rpm). The digested samples were ligated in 1× T4 DNA ligase buffer with 50 U T4 DNA ligase (Roche) at 16°C overnight. The ligated products were treated with 30 μL Proteinase K (10 mg/mL) at 65°C overnight. After reversing the crosslinking, the DNA was purified by phenol-chloroform extraction and precipitated with EtOH. The prepared DNA was digested with 100 U Dpn II (NEB) at 37°C overnight and ligated with 200 U T4 DNA ligase (Roche) at 16°C overnight. The DNA was purified by precipitated with EtOH and GEL/PCR DNA ISOLATION SYSTEM (VIOGENE). 3.4 μg of purified DNA was amplified with specific PCR primers using the Expand Long Range PCR System (Roche) under the following program: 94°C, 2 min; 30 cycles × (94°C, 30 s; 55°C, 1 min; 68°C, 3 min); 68°C, 7 min. PCR products were purified with GEL/PCR DNA ISOLATION SYSTEM (VIOGENE) and were sequenced on Illumina MiSeq instrument using the manufacturer's instructions.

Cell sorting

Cells were infected with influenza virus and subsequently performed virus NP IF as described above. NP negative or positive cells were sorted by cell sorter (MA900, SONY).

DNA fluorescent *in situ* hybridization combined with immunofluorescence

We performed virus NP IF, followed by DNA-FISH, as previously described (Solovei and Cremer, 2010). In brief, we generated probes of PCR fragments of 20 kb from mouse BAC clone of B6Ng01-350C10 and B6Ng01-237E10 (RIKEN BRC), which were labeled using the FISH Tag DNA Kit (Invitrogen life technologies). Cells were fixed and permeabilized, and NP immunostaining was performed using anti-Influenza A Virus NP Ab, followed by post-fixation with 4% paraformaldehyde. Then, we performed pre-treatments for FISH; incubation in 20% glycerol and freezing in liquid nitrogen/thawing for three times, protein removing by 0.1 N HCl, followed by the further treatments; 4xSSC and 50% formamide. The probes were denatured at 75°C, and hybridization was performed at 37°C overnight, in which hybridization mix contained labeled probes, mouse Cot-1 DNA, salmon-sperm DNA dissolved in 50% formamide, 4XSSC and 20% dextran sulfate. After post-hybridization washings, cells were counterstained with Hoechst, and visualized by Nikon A1 HD25 confocal laser scanning microscope. Images were analyzed using NIS-Elements AR Analysis software (Nikon).

Recombinant mouse sFRP2 protein treatment

MEF cells were plated onto 100 mm dish at 80% confluency and treated with 400 ng/μL recombinant mouse sFRP2 protein (R&D Systems) or vehicle (PBS containing 0.1% FBS). After 24 hr, the MEF cells were infected with influenza virus and then subjected to fractionation using cytoplasmic and nuclear fractionation kit (Thermo Fisher Scientific). Each fraction was processed for Western blot analysis.

Cell-cycle arrest

MEF cells were plated onto 150 mm plates at 40-50% confluency. Cells were treated with 2 mM thymidine and incubated for 18 hr. Cells were washed three times with medium and were incubated in fresh medium

for 8 hr. The second thymidine block was applied by adding 2 mM thymidine for 17 hr. Cells were released by washing three times with medium and were harvested 3 hr after the release. Cells were arrested in G0 by 48 hr serum starvation.

Western blotting

Equal amounts of proteins were separated on SDS-PAGE and transferred to a nitrocellulose membrane (Thermo Fisher Scientific) for 60 min at 30V. Membranes were stained with ponceau to confirm protein loading and blocked in 5% skim milk in TBST for 60 min. Membranes were incubated with indicated primary antibodies overnight, washed for at least 45 min in TBST and incubated with horseradish peroxidase conjugated secondary antibodies for 1 hr. Membranes were washed again for at least 45 min and proteins were visualized with ECL prime western blotting detection reagent (GE Healthcare) and detected by a LAS4000 mini (GE Healthcare). The antibodies used in this study are summarized in Table S2.

Quantitative real-time PCR

The mRNA expression levels of PR8 virus NP, and host mRNAs were measured by RT-qPCR. In brief, RNA was extracted from cells using the RNeasy Mini Kit (QIAGEN). First-strand cDNA was synthesized from DNA-free RNA using a Primescript RT reagent kit (Takara). Samples of first strand cDNA were subjected to real-time PCR quantification using Thermal Cycler Dice Real Time System II (Takara) with specific primers for the indicated RNAs with Tbp or 18S as an internal control. Relative amounts of RNAs were calculated by using the comparative C_T method. Primers used in this study are shown in Table S1.

QUANTIFICATION AND STATISTICAL ANALYSIS

For ChIP-seq analysis, reads were mapped to the mouse genome (mm10) using Bowtie2 v. 2.3.4 (Langmead and Salzberg, 2012). Mapping results were piled up using the "samtools sort" command of SAMtools v. 1.11 (Li et al., 2009). To call peaks and compare samples, we used MACS2 v. 2.2.7.1 (Zhang et al., 2008). For CTCF and Rad21, to detect narrow peaks with statistically significance using q-values, we used the following command for each sample: "macs2 callpeak -f BAM -g mm -q 0.01 -B –keep-dup auto -t treat.bam –outdirout_dir", where "treat.bam" was the BAM file of the ChIP-seq mapping result. For other samples, to detect broad peaks, we used the following command: "callpeak –nolambda –min-length 20,000 –max-gap 1000 -f BAM -g mm -q 0.01–keep-dup auto -t treat.bam". To compare Flu- (condition1.bam) and Flu+ (condition2.bam), following command is used: "callpeak –nolambda –min-length 20,000 –max-gap 1000 -f BAM -g mm -q 0.01–keep-dup auto -t condition1.bam -c condition2.bam". After running MACS2, we extracted the peaks with fold enrichment >4, referring to the files of "peaks.xls".

All data are shown as mean ± SEM. Measurements at single time points were analyzed by unpaired t test or analysis of variance with two-tailed t tests. Time courses were analyzed by repeated measurements (mixed model) analysis of variance with Bonferroni post t tests. Log rank tests were performed on Kaplan-Meier survival curves. All statistical tests were calculated using GraphPad Prism 5.00 program (GraphPad). P less than 0.05 was considered to indicate statistical significance. *$p < 0.05$, ** $p < 0.01$.